NORTHWESTERN UNIVERSITY

Measurement of Direct Photon Cross Section in the Forward Pseudorapidity Region at DØ

A DISSERTATION

SUBMITTED TO THE GRADUATE SCHOOL
IN PARTIAL FULFILLMENT OF THE REQUIREMENTS

for the degree

DOCTOR OF PHILOSOPHY

Field of Physics

By
YI-CHENG LIU
EVANSTON, ILLINOIS
June 1996

ABSTRACT

Measurement of Direct Photon
Cross Section in the Forward
Pseudorapidity Region at DØ

YI-CHENG LIU

The production cross section of direct photons in the forward pseudorapidity region has been measured with the DØ detector at the Fermilab Tevatron $p\overline{p}$ Collider. The physics motivation, detecting techniques, and analysis methods are outlined. A cross section is presented, and compared to Next-to-Leading-Order Quantum Chromodynamics calculations. The cross section agrees with the theoretical prediction for transverse energy (E_T) values greater than 30 GeV. At lower E_T the shape of the cross section is steeper than what the theories indicate. The implications and a possible correction of this mismatch are discussed. Further extensions of this measurement are outlined.

Acknowledgements

It has been a long and difficult path to make the measurements presented in this document. Whether I have fulfilled the goals I set out to do is for all to decide. Yet, I could not have gone this far without the kind help of people.

I want to thank the people in the DØ Photon Group, who provided help and inspirations along the way. To Steve Linn, thanks for leading the way in all aspects of the analysis and for providing a nice framework for extracting the all-evasive photon fractions from which I learned a lot. To Paul Rubinov, thanks for the early help to get me started and valuable suggestions later on, as well as the detector maintenance duties he stepped in for me from time to time. To Sal Fahey, I want to express my gratitude for explaining the tricky details to me. I also want to thank John Womersley, as well as Steve Jerger for inspiring discussions. Asher Klatchko also helped me in the early stages of the Monte Carlo studies.

People who gave me their helping hand in the days of my graduate studies in DØ can never be thanked enough. To Rob Avery, Sue Blessing, Jeff Bantly, and Dan Claes, thanks for showing me the way to do various DØ tasks. Rob Avery also helped specifically in the ionization studies for the Forward Drift Chamber, and demonstrated the analytic thinking that has been hard to surpass ever since. I must also pay special thanks to Srini Rajagopalan, who practically was acting as one of my teachers in many things for quite a while.

Special thanks also go to Bruno Gobbi, who showed me what a fully dedicated scientist is like. Most of all, I must thank my thesis advisor, Dave Buchholz, for giving me a chance in this field to begin with, and for all the warm support he provided me all these years, as well as the various ideas and questions he gave me to improve my understanding of detectors and physics. I only hope that I have not let him down on too many occasions.

My wife, Shuhui Lu, has been a constant source of warm support for my daily life

during my graduate studies. Thanks for being so understanding, and so tolerant of my long hours of absence and usual bad mood associated with stress at work.

Finally, I have to pay tribute to my parents. Without their selfless care and intellectual influences from early on in my life I would not even have come this far in my academic career. This thesis is dedicated to them.

Contents

List of Tables

List of Figures

Chapter 1

Introduction

The quantum nature of *photons*, the carriers of electromagnetic interactions, was established almost 80 years ago by Albert Einstein and the founders of Quantum Mechanics. They are copiously produced and thoroughly studied in laboratories. The ubiquitous photon is an integral part in applied sciences, engineering, medicine, defense systems, and other fields in every aspect of modern life. The culmination of our knowledge about photons came in the 1970's when the photons were unified with the W and Z vector bosons to form the family of the *gauge bosons* as the carriers of the fundamental forces which manifest themselves as the electro-weak interactions. There is an enormous amount of experimental data that established the existence and properties of the electro-weak interaction, and the *fermions* they interact with. It is fair to say that photons are one of the most studied and understood of all fundamental particles.

The DØ detector located in the Fermi National Accelerator Laboratory Tevatron collider was designed to be a detector to test and verify the validity of the unifying theory of fundamental particles and their interactions. It can also probe for new phenomena in DØ's extended center-of-mass energy range and detector coverage. The topics pursued in the high-energy collider experiments include the Top quark

(which has recently been discovered in both DØ and the CDF experiments) [1], the precision measurements of the W and Z vector bosons, the production of mesons containing the Bottom quarks, and indications of new phenomena not well described by current theories and models of particle interactions. One particular ingredient of the Standard Model that requires further quantitative investigation is *Quantum Chromodynamics (QCD)*. QCD is the theory that decribes the strong interaction, and is responsible for the production of particles that we eventually observe in the collider detectors. The features of QCD, although qualitatively verified, are far from being completely understood. It is then crucial to investigate the properties of QCD at hadron colliders to probe the inner structure of the hadrons from the standpoint of perturbative QCD techniques and the parton model of strongly interaction particles.

Although photons in general are produced only via electromagnetic interactions, *direct photons* (the topic of this study) are produced at the parton-level in hard collisions. As a result, they contain information about the structure of the hadrons that participate in such collisions. Direct photons enable the physicist a testing ground to understand the validity of QCD and hadronic structures.

Previous experiments have measured the quark distribution functions within hadrons but have had to infer the distribution of gluons indirectly. In $p\overline{p}$ collider experiments like DØ and CDF gluons are major participants in the hard collisions and contribute to the direct photon production processes significantly. Therefore, the measurement of the direct photon production cross section is related to the gluon distribution functions within hadrons.

The DØ detector is designed to be an excellent detector for hadronic hard collisions. One advantage and strength of the DØ detector is that it has nearly complete angular energy measurement coverage around the hard interaction region. It can therefore probe the direct photon production in a kinematic range not currently accessible by other experiments.

It is the goal of this document to describe DØ 's measurement of direct photon

production in the forward region to improve our knowledge of both perturbative quantum chromodynamics and the parton structure within hadrons. The theoretical motivation is elaborated in chapter 2 with a detailed detector description in chapter 3. The experimental strategies and analysis methods are laid out in chapters 4 and 5 with the results and comparisons to theoretical calculations presented in chapter 6, which also concludes with a summary of the analysis and gives some perspectives for future analyses.

Chapter 2

QCD and Direct Photons

2.1 Direct Photons in the framework of QCD

Quantum Chromodynamics (QCD) [2, 3] has been a successful theory in describing the interactions between the fundamental building blocks inside hadrons – quarks and gluons. In addition, it is in good agreement with experimental data collected both at fixed-target and colliding beam experiments. The analysis of enormous amounts of data led us to a deeper understanding of the properties of the fundamental interactions, and also revealed the inner structure of the hadrons. However, the use of perturbative techniques in QCD and its description of the hadronic structures with the parton models still needs further investigation. In addition, the role played by gluons (carriers of the strong interaction) in the hadronic world was inferred indirectly via higher order processes.

The production of high *transverse momentum* photons directly from the parton-parton interactions at the Fermilab Tevatron $p\overline{p}$ collider experiments offers a good general testing ground for the validity of perturbative QCD and for an understanding of the contribution to the hard scatterings from the gluons, in particular. Here, *direct* means that the photons are generated in the hard scattering process, and not

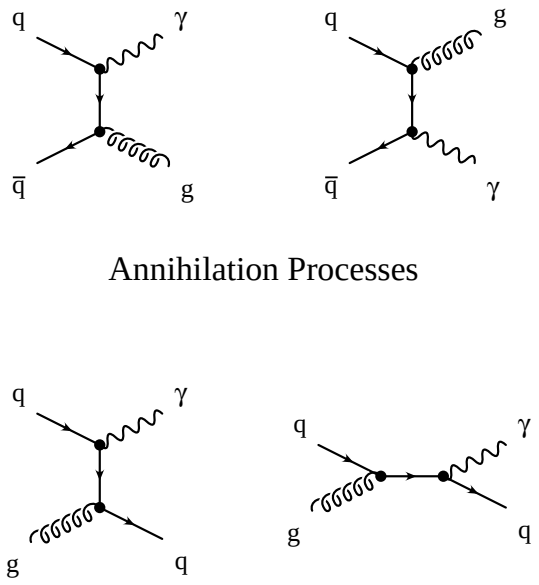

Figure 2.1: Feynman diagrams of leading order ($O(\alpha\alpha_s)$) direct photon production processes.

as the decay or radiation products of the *partons* which take part in the hard scattering. In fact, direct photons offer a complementary channel to study QCD physics, as compared to those normally provided by *jets*, the *fragmentation* products of the hard-scattered quarks or gluons. Pure states of QCD color, like isolated quarks or gluons, do not exist in nature due to the *asymptotic freedom* of the strong coupling constant which leads to color confinement. In the Fermilab Tevatron proton-antiproton ($p\overline{p}$) collider experiments (DØ and CDF), gluons are the major participants of hard collisions at the parton- level, and their contributions to jet and direct photon production are substantial, even dominant in some kinematic regions [4]. This is quite different from deep inelastic scattering (DIS) at either fixed target or e^+e^- collider experiments where quarks are the major participants.

The major contributing physics processes for direct photon production at DØ , to leading order of the strong coupling constant α_s, are the two **annihilation** processes

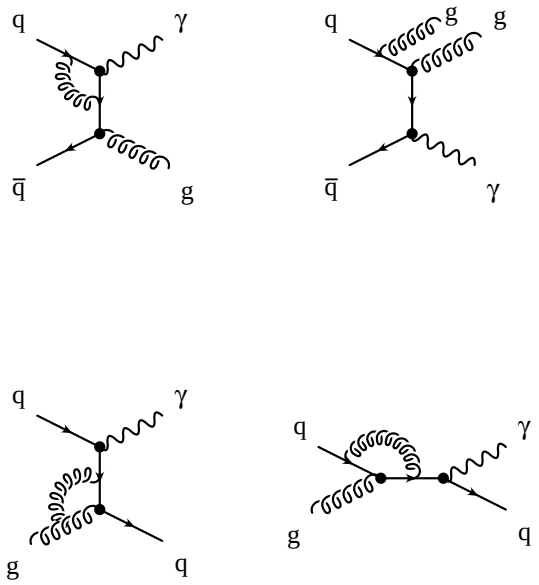

Figure 2.2: A few higher order direct photon production processes which are part of the Next-to-leading-order calculations typically take into account.

and the two **Compton** processes that are shown in figure 2.1. Previous studies indicated that the Compton processes are the dominant ones in the kinematic regions being probed by the Fermilab Tevatron $p\overline{p}$ collider [4, 5].

In recent years, next-to-leading-order (NLO) perturbative QCD calculations have been performed for the direct photon production process, with a few example diagrams shown in figure 2.2. These are processes with extra gluons radiated from the initial or final state partons, or processes with gluon loops as correction to the original leading order process. These considerations in general introduce higher order terms (in the strong coupling constant α_s) into the scattering cross section calculations, which are typically absorbed into either the *renormalization scale* dependence of the strong couple constant, or the *fragmentation scale* dependence of the parton distribution functions [6, 7].

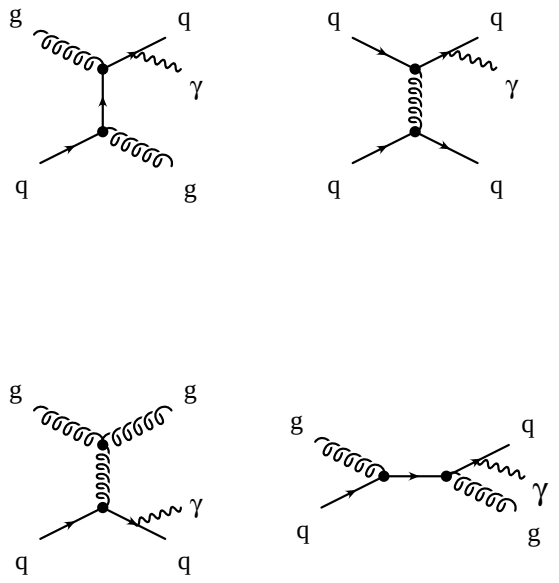

Figure 2.3: Examples of anomalous processes that contribute to the photon production cross section.

In addition to the direct production of photons there are various processes which involve the radiation of fairly high p_T photons from final-state quarks or their fragmentation products, as shown in figure 2.3. In fact, one can obtain the effective fragmentation function of photons from these partons, and therefore include these functions in the calculations of the contributions from these *anomalous*, or *bremsstrahlung* processes. It has been shown [8, 9] that these contribution from the anomalous processes to the photon production cross sections is of the order of $O(\alpha\alpha_s)$, which is comparable to the leading order processes. Therefore, they must be seriously taken into account since experimentally it is difficult to distinguish photons directly produced from the *anomalous* photons. These anomalous processes contribute to the experimentally measured direct photon production cross section. However, a careful choice of a few selection cuts (described later) can usually minimize these contributions.

In general, the number of possible direct photon production processes is far less than that for jet/hadron production at equivalent kinematical energies. In the latter case, various quark flavors each with three colors need to be considered. It is possible to experimentally enhance the direct photon processes over hadronic jet processes in the data sample taken by using specialized triggers. While the inclusive jet production processes are the primary channel to investigate the properties of perturbative QCD, the direct photon channel offer some theoretical as well as experimental advantages relative to inclusive jet processes,

- Photons are in general easier to identify in detectors and the event structure is simpler.
- The measurement of the inclusive photon cross section does not involve the fragmentation processes in the final states.
- Direct photon channels have fewer subprocesses.
- The Compton processes are sensitive to the gluon distributions within hadrons and can in principle be used to constrain these distributions.

However, the measurement of direct photon production has drawbacks and limitations, these include the large proportion of background and relatively smaller production rate compared to jets.

2.2 The QCD-Parton Model Description of the Hard Scattering Processes

The original parton model [10, 7], pioneered by Feynman and Bjorken, was quite successful in describing the data from early deep-inelastic scattering experiments.

Augmented by later developments in perturbative QCD and increasingly sophisticated higher order calculations, the combined QCD-Parton model has been used to lay out the fundamental description of the experimental data and to facilitate comparisons between data and recent theoretical calculations.

At a colliding beam experiment like DØ , the incoming particles and the observed outgoing particles are hadrons instead of individual quarks and gluons. Due to QCD confinement, ie., the interactions between quarks and gluons become infinitely large as the separations between them increase, the only particles we can experimentally observe are the colorless hadrons or leptons coming out as the *fragmentation* products of the original quarks or gluons. Therefore to study the production of high p_T jets or photons, we have to use a model which does an incoherent summation over all possible constituent parton-level scattering processes and then weight these individually by the corresponding parton distribution and fragmentation functions. The schematic of this *factorization* procedure is illustrated in figure 2.4.

In this model, the initial and final state partons that participated in the hard scatterings are assumed to be collinear with the corresponding initial state hadrons. That is, the parton intrinsic transverse momentum, or so-called k_T smearing effect, is not included. As will be shown in later chapters, this effect may have some influence on the measured results and may play a role in the shape of the invariant cross sections.

The separation of parton-level hard scattering and the parton distribution and fragmentation functions is made possible by the *QCD factorization theorem* [3, 11]. According to this the hadronic-level inclusive production cross section can be written down as in equation 2.1 (refer also to figure 2.4), where C is the final state particle one focuses on for inclusive measurements,

$$\sum_{abcd} \int dx_a dx_b dz_c f_A^a(x_a) f_B^b(x_b) D_c^C(z_c) \frac{\hat{s}}{z_c \pi} \frac{d\sigma}{d\hat{t}}(ab \to cd) \qquad (2.1)$$

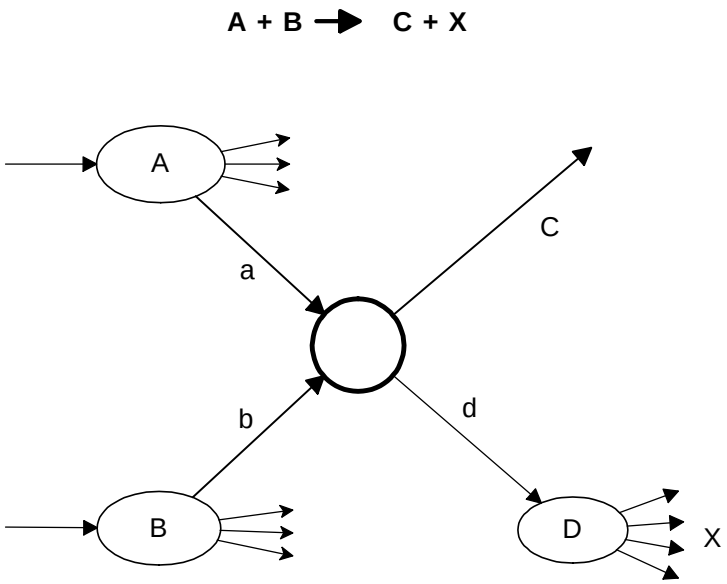

Figure 2.4: Factorization of high E_T photon or jet production processes into parton-level hard scattering convoluted with relevant parton distribution and fragmentation functions for the inclusive processes $A + B \rightarrow C + X$.

In this equation, we have factorized the hadron scattering cross section into the parton-level hard scattering part and the distribution functions of partons within hadrons. Here $f_A^a(x_a)$ describes the probability of finding parton a in a hadron A with momentum fraction between x_a and $x_a + dx_a$ (the same definition applies to parton b). If we are considering the inclusive cross section of a specific final state particle, we also include its *fragmentation* function $D_c^C(z_c)$, which is the probability for obtaining a particle C from parton c with momentum fraction between z_c and $z_c + dz_c$. For the case of direct photon production the situation is simplified a little since we do not need to deal with the fragmentation for an isolated, high p_T direct photon (although one can still incorporate the contributions from the anomalous processes in the effective photon fragmentation function). However, *photon-like* particles in the detectors can also come from the fragmentation products of partons, or the decay products of neutral mesons which result from fragmentation processes.

The parton-level hard scattering cross section $\frac{d\hat{\sigma}}{d\hat{t}}$ is in general an incoherent sum of all participating subprocesses, each of which is convoluted or weighted with the corresponding parton distribution functions. Here, the relative merit of the direct photon processes is twofold – they generally include fewer contributing processes and the event structure is not obscured by the presence of the extra fragmentation processes.

2.3 Coordinate System and Kinematical Variables

This section will define the coordinate system used when describing the physics events and the various kinematic variables which are crucial to the description of both the events and the detector systems.

For a relativistic particle with four–momentum (E, P_x, P_y, P_z), the *rapidity* is defined to be,

$$y = \frac{1}{2} ln \frac{E + P_z}{E - P_z}. \tag{2.2}$$

In the case where particles are very relativistic, namely their rest masses are much smaller than their momenta, the rapidity can be approximated well by the *pseudorapidity* η,

$$\eta = -ln(tan\frac{\theta}{2}). \tag{2.3}$$

Therefore, in this document all references to rapidities are made in terms of pseudorapidities with the understanding that the above approximation is valid. It is worth emphasizing here that the multiplicity distribution of the soft particles of the underlying minimum-bias event is roughly uniform in pseudorapidity.

We assume that the incoming hadrons of the collision processes are along the z and $-z$ coordinate directions. The polar angle from the z-axis is the angle θ which has a one-to-one correspondence with the pseudorapidity η. The azimuthal angle is measured relative to the positive x-axis direction.

As shown in figure 2.4, the final state particle C, either a photon or a parton (which then goes through the fragmentation process and materializes as a jet of hadrons), is the one we actually try to measure in the experimental inclusive study. If this final state particle has transverse momentum p_t, its energy-momentum 4-vector is related to the pseudorapidity η and p_T by the following relationship,

$$p_C = p_t(cosh(\eta), 1, 0, sinh(\eta)) \tag{2.4}$$

The relativistically invariant Mandelstam variables of the hadronic collisions are defined to be,

$$s = (p_A + p_B)^2, t = (p_A - p_C)^2, u = (p_B - p_C)^2 \tag{2.5}$$

with the corresponding variables given for the hard scattering parton-level processes,

$$\hat{s} = x_a x_b s \tag{2.6}$$

$$\hat{t} = -x_a p_T \sqrt{s} e^{-\eta_a} \tag{2.7}$$

$$\hat{u} = -x_b p_T \sqrt{s} e^{\eta_a} \tag{2.8}$$

which appear frequently in the expressions of various parton-level cross sections.

2.4 Calculations of Direct Photon Production by NLO Perturbative QCD

The theoretical doubly-differential inclusive direct photon production cross section can be conveniently split into three major terms [8],

$$\frac{d^2}{dP_T dy}\sigma_{full} = \frac{d^2}{dP_T dy}\sigma_{LO} + \frac{d^2}{dP_T dy}\sigma_{HO} + \frac{d^2}{dP_T dy}\sigma_{AN} \tag{2.9}$$

in which, LO stands for lowest order contributions, HO higher order contributions, and AN anomalous contributions due to radiation of photons from final state quarks.

As we proceed in elaborating about the features of this cross section, we will show that by adopting an experimental *isolation cut* on the photon candidates, we can reduce the relative importance of the anomalous term in the cross section. This method is based on the expectation that direct photons from hard scattering are fairly isolation in the detector, while photons from anomalous contributions usually have quite a few hadrons in their vicinity coming from fragmentation products of the final state parton. A schematic illustration of this method is shown in figure 2.5.

Experimentally, the doubly-differential inclusive direct photon production cross section is obtained by the following equation :

$$\frac{d^2\sigma}{dP_T \cdot d\eta} = \frac{\alpha \cdot N}{L \cdot A \cdot \varepsilon \cdot \triangle P_T \cdot \triangle \eta} \tag{2.10}$$

where α is the experimental photon fraction or purity, L is the integrated luminosity, A is the detector acceptance, and ε is the efficiency for detecting photons. The experimental measurement of the photon cross section requires an isolation cut for the energy distribution around the experimental photon candidates. This is equivalent to drawing two cones of pre-defined radii $\delta\ R$ where,

$$\delta\ R = \sqrt{\delta\eta^2 + \delta\phi^2} \tag{2.11}$$

and defining the energy deposition cut values for the energy falling in the area between the two cones.

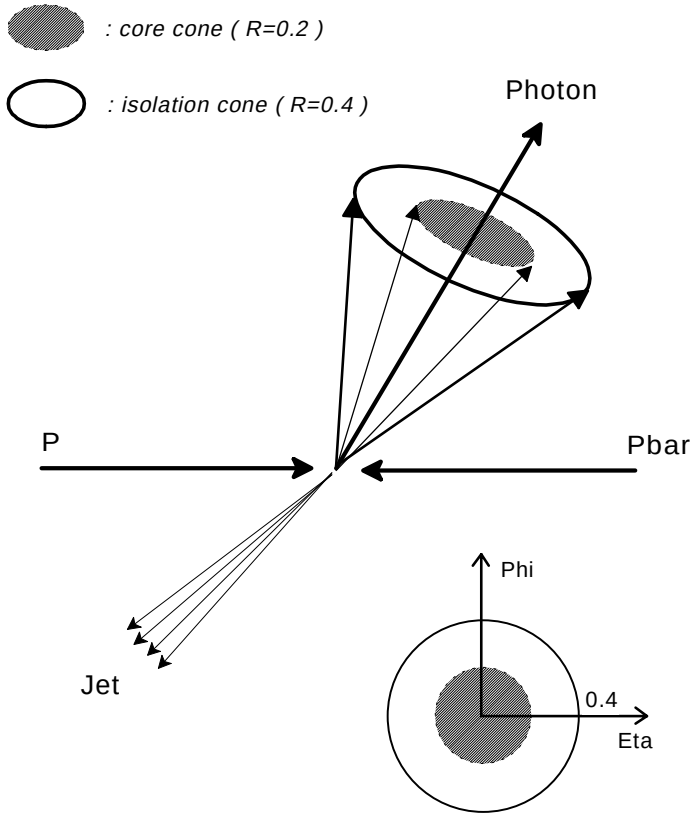

Figure 2.5: Isolation method for reducing the contribution from the anomalous processes.

A similar isolation cut criteria is implemented in theory by modifying the anomalous contribution to the total cross section, since only in the anomalous, processes are photons associated with nearby hadronic activities. We want to compare results from different experiments and to make theoretical models flexible to be able to accommodate additional physics processes (jets as well as photons). The isolation cut is included in the anomalous portion of the cross section in a flexible and easily modified way in the isolation area definitions. The pseudorapidity region and p_T range can also be conveniently modified for comparisons. Therefore, the experimental measurement of the single direct photon production cross section can be compared to one of these specific sets of theoretical predictions with equivalent isolation cuts [8].

Leading order QCD calculations of various large transverse momentum photon production processes suffer unavoidably large theoretical uncertainties due to the sensitivity of the renormalization and factorization scales. It was pointed out that Next-to-Leading-Logarithm calculations are needed to improve the scale dependence [12]. In recent years, Next-to-Leading-Order (NLO) QCD calculations of direct photon cross sections and their behavior have been reported by various theoretical groups [8, 13]. These calculations take into account both leading-logarithm and next-to-leading-logarithm approximation, and were shown to be less sensitive to the scale dependences of the strong coupling constant and the parton distribution functions. However, the scales still have to be unambiguously specified since they come in as parameters in the strong coupling constant and parton distribution functions. Various attempts have been made to reduce this remaining scale sensitivity. Some groups adopted the so-called *Principle of Minimal Sensitivity* in the NLO calculations by requiring the following relationships,

$$M \frac{\partial \sigma}{\partial M} = 0 \tag{2.12}$$

where M is the factorization scale, or,

$$\mu \frac{\partial \sigma}{\partial \mu} = 0 \tag{2.13}$$

where μ is the renormalization scale.

Other groups have simply adopted a typical momentum scale in the production processes of high transverse momentum jets or photons. Some scale dependences still remains in the theoretical predictions and it is up to the experiments to indicate which may be a better optimization scheme for their data.

2.5 Relationships with Parton Distributions

After the parton-level cross sections are calculated, the overall hadron-level cross section is obtained by convoluting with parton distribution functions f_Q^qs as shown in equation 2.1. To match what is observed experimentally, namely jets, a further convolution has to be applied by including the fragmentation functions of the partons. These are obtained phenomenologically and can not be obtained from first principle calculations.

In processes that have a photon coming directly from the hard collision and an accompanying quark or gluon (figure 2.1), the complexity of the event is reduced by having fewer jets in the events. This is clearly an advantage since the identification of jets is more ambiguous than the identification of photons.

Previous analyses of deep inelastic scattering (DIS) experiments have obtained reasonable estimates of the parton distribution functions within hadrons. Yet, gluons enter the DIS processes only as second order effects since they do not participate in the electromagnetic or weak interactions which are the primary processes taking place in deep inelastic scatterings. Their behavior cannot be well determined by DIS analysis. On the other hand, in very high energy $p\overline{p}$ collisions gluons have very large contributions, and therefore provide a good testing ground for gluon distributions.

2.6 Uniqueness of the Forward Region

As previous theoretical investigations showed [8], the cross section of direct photons has a pseudorapidity dependence which is sensitive to the parameterization of the gluon distribution functions. This sensitivity is even more dramatic in the lower transverse momentum or in the forward regions of the detector. Since most earlier experimental direct photon results have focused on the central pseudorapidity region, the forward direct photon detection capability of the DØ detector allows us a new region for investigating the pseudorapidity dependence where gluon distribution within hadrons can be constrained. This motivation is based on the fact that the transverse momentum fraction probed by the photons (or jets in a general sense) is

$$x_T = \frac{2p_T}{\sqrt{s}}. \tag{2.14}$$

In addition, the minimum momentum fraction x of the hard scattering partons within the incoming hadrons that can be probed with inclusive measurements is roughly

$$x_{min} = \frac{x_T e^{-\eta}}{2 - x_T e^{y}}. \tag{2.15}$$

This is more crucial for the case of gluons since their momentum fraction distribution peaks at lower x values [14]. As one goes to lower p_T or pseudorapidity η, there is an increased possibility to study gluons near the x range around 0.001 where they are dominant in the hadronic structures [12, 15]. One can refer to figure 2.6 which shows explicitly the gluon x range probed given an experimental p_T and pseudorapidity coverage.

2.7 Window to a New World ?

Other than being a good testing ground of recent NLO QCD calculations, the direct photons observed at the collider experiments like DØ and CDF can help us in search-

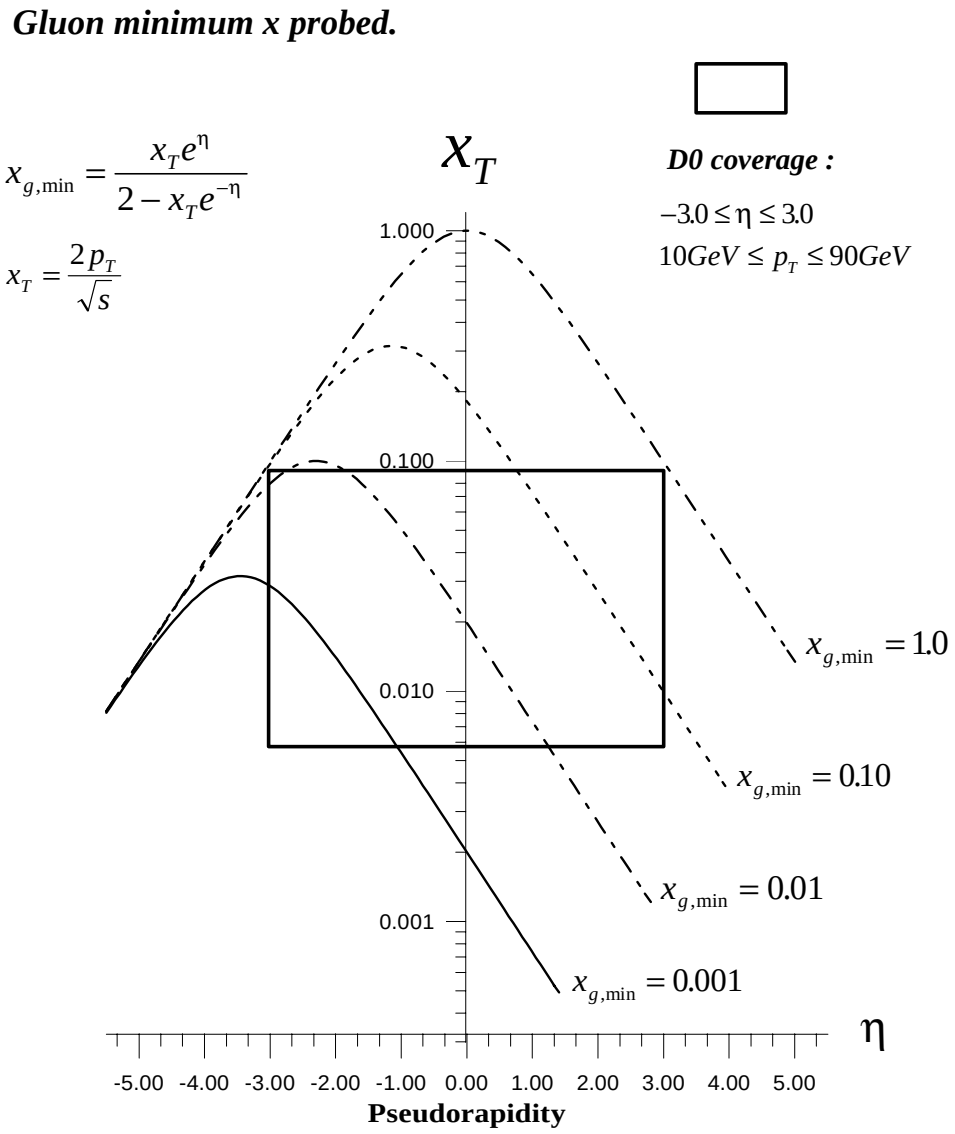

Figure 2.6: The gluon x values probed by experiments with various x_T and pseudorapidity coverages. Contour lines mark constant values of minimum gluon x probed.

ing for exotic phenomena like the excited quark states,

$$q + g \rightarrow q^* \rightarrow q + \gamma \tag{2.16}$$

On the other hand, in the search for the Higgs particles that are responsible for the spontaneous breaking of the electro-weak gauge symmetries and the generation of quark and lepton masses in the minimal standard model of elementary particle interactions, photons play an important role since the di-photon signal is a unique signature of the neutral Higgs decay process,

$$H^0 \rightarrow \gamma + \gamma \tag{2.17}$$

Although this is not the dominant channel of Higgs decays (in fact its branching ratio is relatively small), the two photons are readily detectable in existing detectors. If the neutral Higgs particles turned out to have lower mass than previously expected, this di-photon decay channel is accessible with current facilities and in future detectors at CERN LHC collider experiments. One needs to be able to understand the background contributions from parton- level di-photon production, direct photon plus single-bremsstrahlung, double- bremsstrahlung, and higher order box productions of di-photons [5].

Most other experiments have either concentrated exclusively in the central pseudorapidity region, or had much lower center-of-mass energies. By having a unique coverage of the forward pseudorapidity region, the DØ detector can investigate the various photon channels in a wider range, and may be able to observe the above mentioned new phenomena.

Chapter 3

The DØ Detector

3.1 Overview

The DØ detector is designed to have excellent performance for studying various physics processes in the Fermilab Tevatron $p\overline{p}$ colliding beam environment. It emphasizes the detection of high transverse momentum phenomena with efficient electron and muon detection, good jet identification, and full solid angle coverage to minimize energy loss from neutrinos which show up as missing transverse energy in the detector. These goals were achieved by having a hermetic, radiation-hard, finely-segmented calorimeter, and a compact non-magnetic central tracking systems. A perspective view of the entire detector with a partial cut-away to the inner layer is shown in figure 3.1. A detailed description along with a summary of relevant properties of all the DØ detector subsystems is given elsewhere [16].

For general QCD analysis, the main requirement is the identification of fragmentation jets from hard-scattering partons as well as high transverse momentum photons. Therefore, the uranium liquid argon sampling calorimeter subsystems with good energy measurement resolution are the main detectors used in this analysis. The calorimeters are finely segmented to detect the detailed structure of the elec-

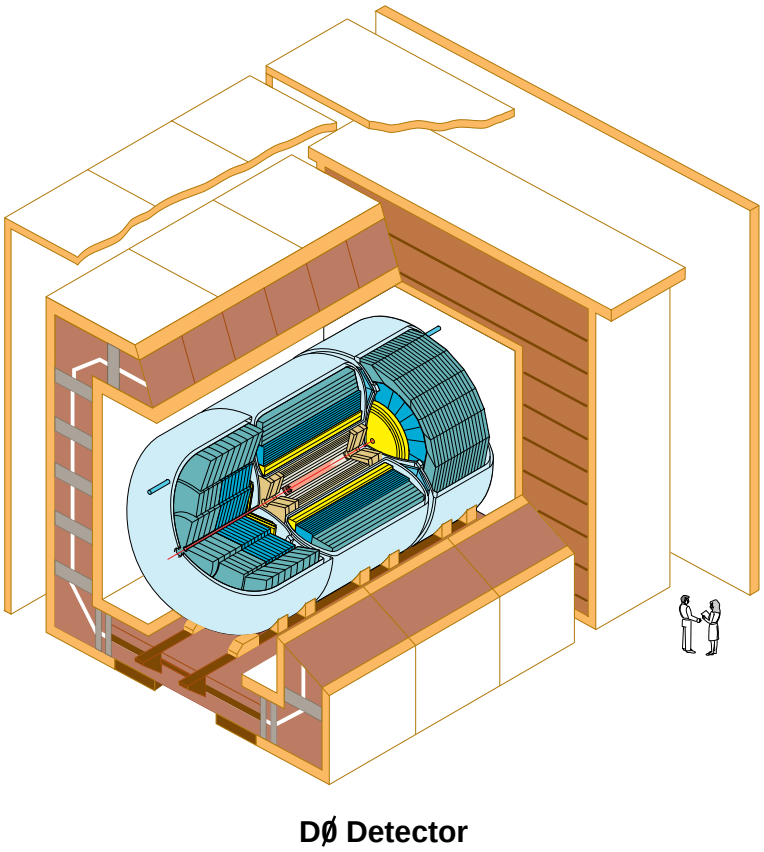

Figure 3.1: 3-D and partial cut-away view of the DØ Detector.

tromagnetic and hadronic showers. For studying the production of high p_T direct photons, the tracking subsystem was also used for statistically rejecting background contributions mainly from neutral π^0 and η mesons which decay into photons.

A brief summary of the detector subsystems will be given here, with particular emphasis on the components which were used in the analysis of direct photon production in the forward pseudorapidity region. These include the Forward Drift Chambers (FDC, which has two separate halves, North and South), and the Electromagnetic End Calorimeters (EC, which also has two halves.)

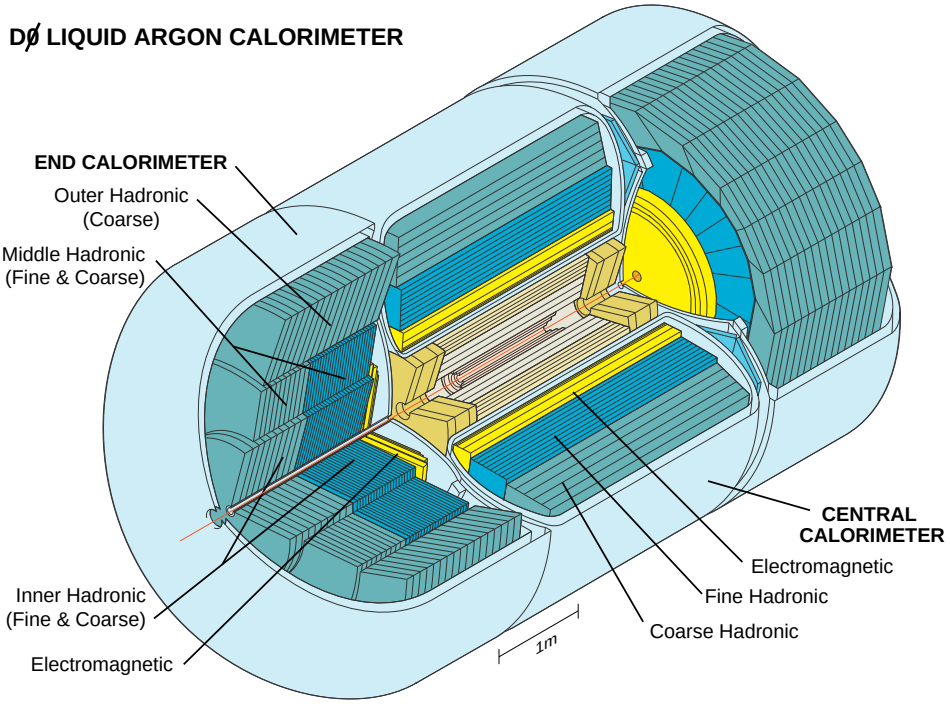

Figure 3.2: The DØ Calorimeters.

3.2 Calorimeters

The DØ calorimeter system [16, 17] consists of 3 cryostats which enclose the Central Calorimeter (CC) and the two halves of the End Calorimeters (EC). Due to the absence of a magnetic toroid within the tracking region of the DØ detector, the whole calorimeter system is rather compact, radiation-hard, and hermetic. Liquid argon is used as the active media within the calorimeters for sampling and measuring the energies of particles traversing the calorimeters. The calorimeter modules are enclosed within 3 separate sets of cryostats to be able to access the tracking detectors. A cut-away view of the whole calorimeter subsystem is given in figure 3.2.

Both the Central and End Calorimeters contain electromagnetic and hadronic sections. The electromagnetic sections of the End Calorimeters were mainly used

for the forward direct photon studies. The following is a detailed description of the calorimeter configurations.

Central Calorimeter : $|\eta| < 1.2$

- Electromagnetic : Consists of multi-module, multi-layer depleted uranium plates acting as absorbers which are separated by gaps filled with liquid argon as the active media for ionization detection and sampling. The main function of the Electromagnetic Calorimeter is to fully contain and measure the electromagnetic showers produced by primary electrons and photons.
- Fine Hadronic : Consists of thicker uranium absorbers separated by liquid argon. The Fine Hadronic section serves to identify the showers due to hadronic interactions.
- Coarse Hadronic : Consists of copper plate absorbers separated by liquid argon. The Coarse Hadronic section serves to measures whether energy leaks out of the Fine Hadronic section and also serves as a shield for the Muon chambers.

End Calorimeter : $1.4 < |\eta| < 4.5$

The End Calorimeter is designed to cover the forward pseudorapidity region between $1.4 < |\eta| < 4.5$ with full azimuthal coverage. It is subdivided into the following sections :

- Electromagnetic : This uses uranium plates as the absorbers (except for the very first two plates which were made of stainless steel to be more sensitive to the showers initiated within the cryostat walls which are just in front of the End Calorimeters) for a total of 20.13 radiation lengths.
- Inner Fine Hadronic : This uses uranium as the absorber, 121.84 radiation lengths.

- Inner Coarse Hadronic : This uses uranium as the absorber, 32.78 radiation lengths.
- Middle Fine Hadronic : This uses uranium as the absorber, 115.52 radiation lengths.
- Middle Coarse Hadronic : This uses stainless steel as the absorber, 37.95 radiation lengths.
- Outer Hadronic : This uses stainless steel as the absorber, 65.07 radiation lengths.

Since the forward direct photon analysis relies heavily on the electromagnetic section, a detailed description of the sections used for photon detection and background estimation is given in a later section.

Between the Central and End Calorimeters, there is the Inter-Cryostat Detector (ICD) to correct for the energy loss in the uninstrumented (cryostat walls, endcaps) region. The ICD consists mainly of scintillator tiles 0.1x0.1 in η-ϕ with phototubes for readouts. They offer an adequate approximation of the electromagnetic showers in this region.

3.3 Central Tracking Detectors

The DØ Central Tracking System [16, 18], shown in figure 3.3, occupies the region between the tevatron beam-pipe and the inner walls of the Electromagnetic Calorimeters. It was designed to have good spatial resolution, two-track resolving power, high efficiency, and good ionization energy measurements. Since there is no magnetic field in the tracking region, we rely on the calorimeters for energy measurements.

The central tracking subsystems consist of the following subdetectors :

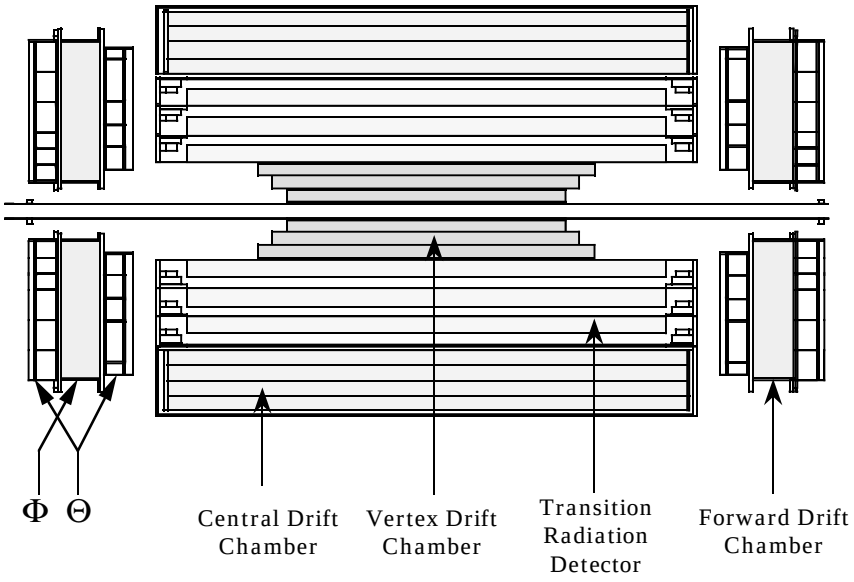

Figure 3.3: Side view of the DØ tracking detectors.

Vertex Chamber (VTX)

This consists of 3 concentric layers of drift cells where the wires are axial and parallel to the beam direction. The Vertex Chamber's primary purpose is to identify tracks very close to the interaction region, and most of all, to identify the primary interaction point. The longitudinal position along the Vertex Chamber is obtained by the charge division method. Since the sense wire is resistive, the position is obtained by comparing the integrated pulse areas from both ends of the sense wire. The Vertex Chamber is generally used in this analysis for primary vertex identification. Since its end-cap extends into the forward pseudorapidity region where our physics interests are, we need to estimate the contribution of the Vertex Chamber material to the conversion of photons.

Transition Radiation Detector (TRD)

This is capable of distinguishing electrons from other charged hadrons. It consists of three layers, each with 382 X-ray radiating polypropylene (C_2H_2) foils

in layers filled with nitrogen gas. It uses the fact that radiation is emitted when a charged particle traverses layers of materials of different dielectric constants. The characteristics of the emitted X-ray radiation, mainly the intensity and angular distribution, depend on the particle energy to mass ratio, which makes particle identification possible. The X-ray detection is accomplished with a radial-drift PWC after the radiator where the X-rays convert and the ionization from the charged particles are collected on the sense wires. The detecting volume utilizes the gas mixture $Xe(91\%)/CH_4(7\%)/C_2H_6(2\%)$. Overall, the TRD has a pion rejection factor of approximately 50 for 90% electron efficiency.

Central Drift Chamber (CDC)

The CDC consists of 4 cylindrical layers of drift cells and covers roughly the pseudorapidity region $|\eta| < 1.1$. It provides radial and longitudinal information for track identification. It is also used to identify the primary interaction vertex, as well as to provide track ionization information. It uses a gas mixture $4\%CH_4, 3\%CO_2, 93\%\, Argon$. Each drift layer is segmented into 32 separate drift cells. The sense wires are strung in the longitudinal direction, along the beam. Each cell also has two delay lines near the first and last sense wires to provide longitudinal position information. The Central Drift Chamber is the main subdetector used for direct photon background estimation in the central pseudorapidity region. Since it does not overlap in the polar coordinates with the Forward Drift Chamber, it does not provide information for forward direct photons. However, the less crowded environment in the Central Drift Chamber proved to be a better testing ground for the same analysis procedures used in both the central and forward regions. As a result, most of the analysis schemes to be described in the following chapters were verified first in the central region, and then modified for use in the forward region.

Forward Drift Chamber (FDC)

The FDC covers roughly the pseudorapity region $1.5 < |\eta| < 3.0$. It is crucial in this analysis for providing the ionization information of charged particles for photon channel background estimations. A separate section is given later with a detailed description of this chamber.

3.4 Muon Systems

The DØ Muon subsystem is the final detector. It encloses the entire central tracking and calorimetry regions. There are two major parts in the Muon subsystem : the Wide Angle Muon System (WAMUS) and Small Angle Muon System (SAMUS). They consist mostly of proportional drift tubes (PDT) to detect muons which penetrate the calorimeters without being stopped. A solid-iron toroidal magnet between the inner and outer layers of the Muon chambers permits a determination of the muon momenta. The Muon subsystem is not used for the photon analysis as all photon-like particles would have been completely contained in the calorimeters.

3.5 Trigger Systems

To cope with the high event rate at a typical luminosity of the order of $L = 5 \times 10^{30} cm^{-2} s^{-1}$ and still be able to trigger on interesting physics events, DØ is using a three level, increasingly sophisticated, strategy for the triggering system.

- Level-0 consists of scintillation counters on the front surfaces of the End Calorimeters to tag the occurrence of inelastic collisions and also serve as the instantaneous luminosity counter.

- Level-1 uses the analog and digital information available within the $3.5 \mu s$ between collider bunch crossings. The Level-1 subsystem provides fast hardware estimation of the energy deposition in the calorimeter by summing energy in

trigger towers of 0.2x0.2 in (η ,ϕ) space. The photon analysis relies on the level-1 calorimeter triggers to locate events with high p_T photons.

- Level-2 : The next level of software filtering is provided by a set of parallel processors collectively called the Level-2 farm. It consists of DEC VAXStations using the DEC VAXELN real-time multitasking system to run the online filters. Each event is sent to a separate VAXStation to calculate properties like the calorimeter energy clusters, missing transverse energies, approximate muon and jet identification, and charged tracks [19] in the central tracking chambers. The software filters mark the corresponding filter bits in the data stream for later data streaming and processing. The photon analysis presented here utilized various dedicated photon level-2 filters to mark potentially good photon events for off-line processing.

Since there are huge differences in the cross sections of various physics processes, some dominant trigger/filters usually have to be pre-scaled so that all physics channels can have reasonable amounts of data. The low E_T photon data were actually done in special runs with a dedicated trigger because the cross section is high.

3.6 Detector Components Crucial for the Direct Photon Analysis

Figure 3.4 shows a cut-away view of the DØ calorimeter and tracking subsystems which shows the radial depths as well as lines marking separations in pseudorapidity. Monte Carlo detector simulations were performed to study the photon conversion probabilities over the forward pseudorapidity range. $1.6 < |\eta| < 2.5$ was finally chosen for direct photon production cross section measurements due to its relative uniformity in conversion probability. The conversion probability pseudorapidity distribution will

be elaborated in more detail in chapter 4.

3.6.1 The Forward Drift Chamber

The forward drift chamber (figure 3.5) is designed to cover the pseudorapidity region of $1.3 < |\eta| < 3.0$ and to provide tracking capability in this important yet difficult region. Each of the two chambers (one on the north and one on the south side) consists of 3 layers with two **Theta** chambers sandwiching one **Phi** chamber. Each Theta chamber is further divided into 4 quadrants each with 6 drift cells. Within each cell the sense wires are strung perpendicular to the beam direction with the wire planes parallel to the beam direction. In the Phi chamber there are 36 radial cells distributed evenly in azimuth with the radial sense wires perpendicular to the beam. Each sense wire is separated from the adjacent sense wire by electric field shaping guard wires. There is also one delay-line in each Theta cell to provide the position of the tracks along the sense wire direction.

Each Theta chamber cell measures eight positions along the tracks, and therefore provide the θ orientation of the tracks, while the ϕ coordinates are provided by the 16 positions along the track measured by the Phi modules. All sense wires in both type of cells are staggered by $\pm 200\mu$m to resolve the left-right ambiguity. The chamber is operated at atmospheric pressure with the gas mixture $3\%CO_2, 4\%Methane, 1.2\%H_2O$, and $91.8\%Argon$. There are various high voltage configurations for the **Theta** chambers. Negative high voltage of around 4.75 k volts is applied on the field shaping electrodes to provide a constant drift field across the Theta drift cells, while positive high voltage of around 1.53k volts is applied to the sense wires. The sense wires next to the delay-lines have a slightly higher voltage of 100 volts to achieve more gain and hence better signals in the delay lines . The guard wires are kept at ground potential. The sense wires in the **Phi** chambers are kept at 1.450 k volts with field shaping voltages at -3.8 and -3.4 k volts.

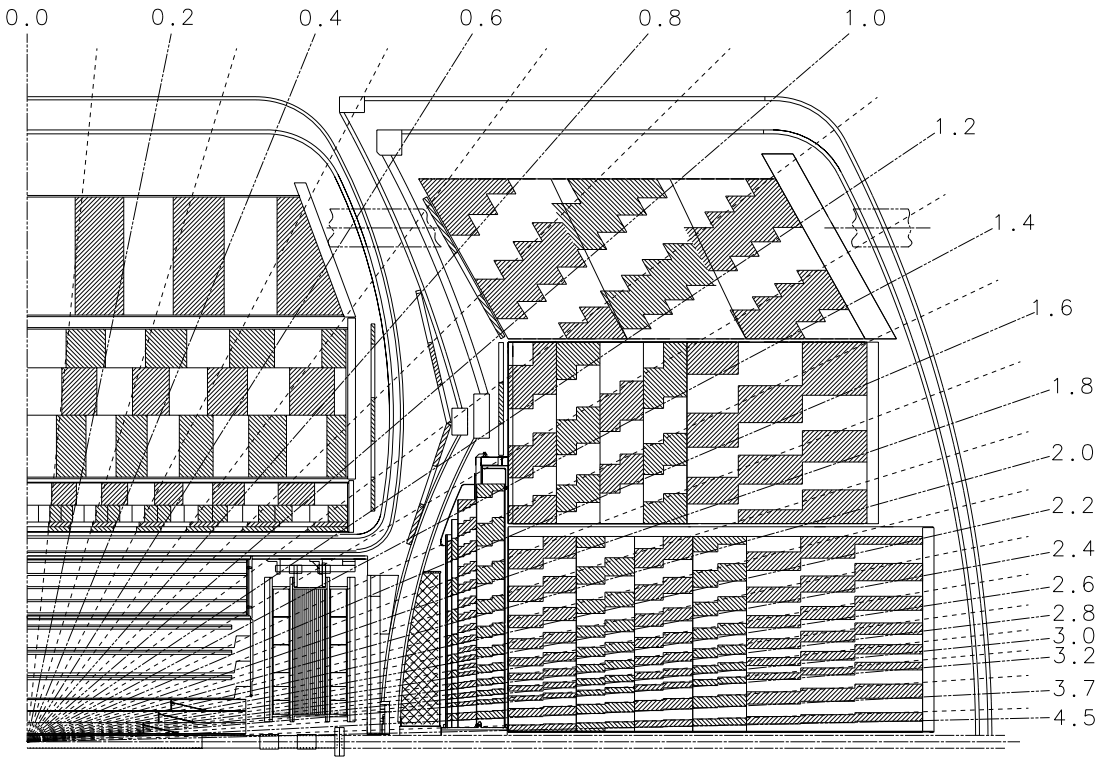

Figure 3.4: Side view of DØ tracking and calorimeter systems showing the transverse and longitudinal segmentation patterns. The lines mark various regions in pseudorapidity. The forward photon study in this document focuses on the region $1.6 < |\eta| < 2.5$.

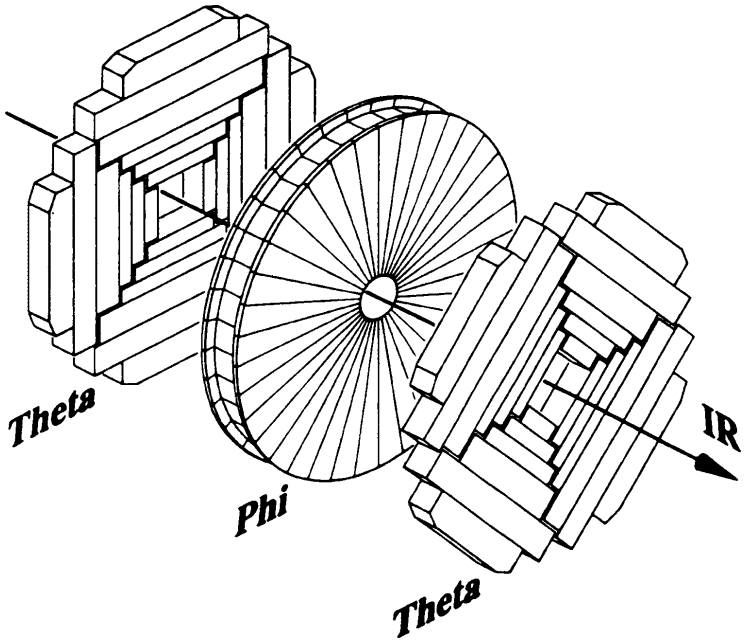

Figure 3.5: The Forward Drift Chamber.

Early test beam and cosmic ray data showed that the forward drift chambers had an overall spatial resolution of approximately 200 μm [20]. Monte Carlo single track simulations and collider data from W and Z boson subsamples were both used to study the efficiencies of the track-finding algorithms. A few FDC performance parameters measured by test beam studies are summarized in table 3.1.

During Run 1A, a small portion of water vapor (0.5 %) was introduced into the chamber to alleviate the radiation aging effects. It is expected that part of the aging is due to dark current - emission of secondary electrons from cathode surface charge build-up. Small amounts of water are supposed to be able to make the surface deposits slightly conductive and reduce the charge build-up rate. The gas flow rate was also increased to reduce build-up and deposits. Data showed that the rate of aging has decreased due to the increase in gas flow and the introduction of water vapor.

FDC is useful in this direct photon analysis not only to tag the electromagnetic

Table 3.1: Forward Drift Chamber Performance.

FDC Performance Parameters	
Spatial Resolution	200 μm
Hit Finding Efficiency	95%
Two Hit Separation	2.4 mm at 90% eff.
dE/dX Resolution	13%
2 MIP Rejection Factor	85 at 90% eff.

candidates as either *photon-like* (no-track) or *electron-like* (with-track), but also to provide the track ionization information. This capability will be used as a discriminator to statistically estimate the fractions of photon-like and background-like events and will be described fully in chapters 4 and 5.

3.6.2 The Electromagnetic End Calorimeter (ECEM)

The electromagnetic section of the End Calorimeter is the most crucial one for this analysis. Photons are detected as electromagnetic showers of cascading bremsstrahlung and pair-creation processes within the calorimeters. Referred to as *ECEM*, it consists of layers of absorber plates made of 2 mm thick depleted uranium. Liquid argon fills the 2mm gaps between the plates and acts as the active media for ionization measurements. Coated G-10 signal readout boards are located within the liquid argon gaps. The combination of an absorber plate, the liquid argon gap, and the signal board makes a basic sampling cell. Eighteen cells then make up the whole electromagnetic End Calorimeter module. The electromagnetic showers develop within the absorber plates, and the ionization in the liquid argon is measured by collecting the charges on the signal readout boards. Overall, the ECEM contains approximately 20 radiation

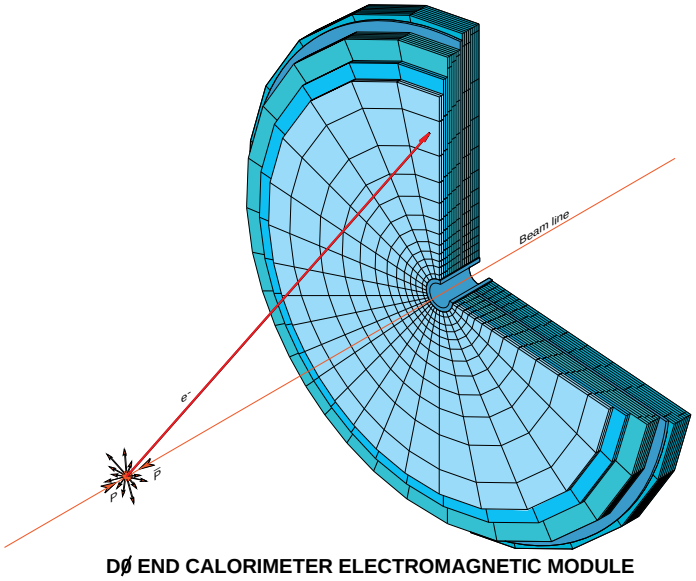

Figure 3.6: The Electromagnetic End Calorimeter.

lengths at normal incidence.

The layout of the electromagnetic section of the End Calorimeter is clearly shown in figure 3.6. A typical hadronic collision and a particle coming from the interaction point are also shown to indicate the semi-projective nature of the calorimeter towers.

Longitudinally, the End Electromagnetic Calorimeter is divided into four readout layers. The electromagnetic shower maximum normally occurs within the third layer. The transverse segmentation of the ECEM is similar to that of the Central Calorimeter, namely 0.1x 0.1 in η-ϕ space, but the third EM layer is further segmented in η-ϕ to 0.05x0.05. This fine transverse segmentation is provided by the configuration of the readout pad electrodes on the signal boards, which result in semi-projective readout *towers* representing the electromagnetic showers within the calorimeter.

The DØ calorimeters were all tested and calibrated in a Fermilab test beam fa-

cility. Since the calorimeters measure the energies by sampling and this is a statistical process with the number of samples proportional to the energy E, the energy resolution is generally proportional to $\sqrt{E}$. This means that the fractional energy resolution is proportional to $\frac{1}{\sqrt{E}}$. Early results [17] showed that the Electromagnetic End Calorimeters have a relative resolution as a function of energy,

$$(\frac{\sigma_E}{E})^2 = C^2 + \frac{S^2}{E} + \frac{N^2}{E^2} \tag{3.1}$$

where the calibration error C is 0.003 ± 0.002, the sampling fluctuation S is $0.157 \pm 0.005\sqrt{GeV}$ for electrons, and the noise contribution N is $0.29 \pm 0.03(GeV)$. The position resolution of the ECEM varies approximately with as $\sqrt{E}$.

The showers from various objects like electrons, pions, as well as Monte Carlo simulated particles were compared and their corresponding shape differences were studied. These shower shape profiles are then used in the off-line reconstruction and analysis software for the identification of electrons, photons, and jets.

Chapter 4

Experimental Issues

4.1 Pre-analysis Considerations

The forward direct photon data reported here were taken during the 1992-1993 Collider RUN 1A. It was the initial data taking period for the DØ detector in the colliding beam environment. During that first year of running we were studying the newly acquired data to determine how well the detector performed in the high beam luminosity environment. This was compared with previous detector calibrations to understand how we could get consistent parameter descriptions for various physical objects such as electrons, muons, and jets [21]. We started to see how various physics events appeared in the detector and began fine-tuning the analysis procedure to extract physics results.

Unlike rare physics channels like W and Z gauge bosons, the direct photons are produced abundantly through QCD/QED processes. In order not to overwhelm the data-taking bandwidth, the triggers with possible photon candidates have to be prescaled. The total cross section for $p\overline{p}$ interactions at $\sqrt{s} = 1.8$ TeV is 72.1 ± 3.3 mb, while the total cross section of the direct photon events is about 10 nb. In the second half of the collider RUN 1A, 18 special runs were also taken with dedicated photon

triggers to populate the lower E_T spectrum which had been heavily pre-scaled during normal running. In general, the off-line data processing procedures put the direct photon event data in the ALL stream global data sets and the special run data sets. The raw data sets were processed at the off-line computing workstation farm with the DØ reconstruction program D0RECO version 11.19. Physics parameters were reconstructed, structurally organized, and written onto various Data Summary Tape (DST) files for further physics analyses.

Figure 4.1 gives an illustration of the direct photon data analysis procedures. From the preliminary data samples on the DST files a first stage analysis was performed to locate photon-like candidates. The relevant properties of these candidates were written to compact data files in *Ntuple* format. The Ntuples were then selected by the trigger/filter criteria and by a detector fiducial area cut. Event selection cuts were then fine-tuned to locate a sub-sample of events containing cleaner photon candidates. Since two separate analysis methods were used to estimate the fractions of direct photons and background particles, a set of discriminating cuts for each corresponding method was applied that separated the data into two different samples.

In the following we describe the characteristics of the direct photon events and highlight a few key points in the analyses.

4.2 Event Structure

As can be seen from the Feynman diagrams in chapter 2 showing the dominant direct photon processes, the majority of the direct photon events are accompanied by one or more jets [22]. On the parton level the production of a direct photon is invariably accompanied by a quark or gluon. Due to color confinement, these quarks and gluons go through the fragmentation processes and show up in the detector as jets of hadrons.

An isolated photon candidate may or may not have a track associated with it, since there is a finite probability for the photon to convert in the detector volume

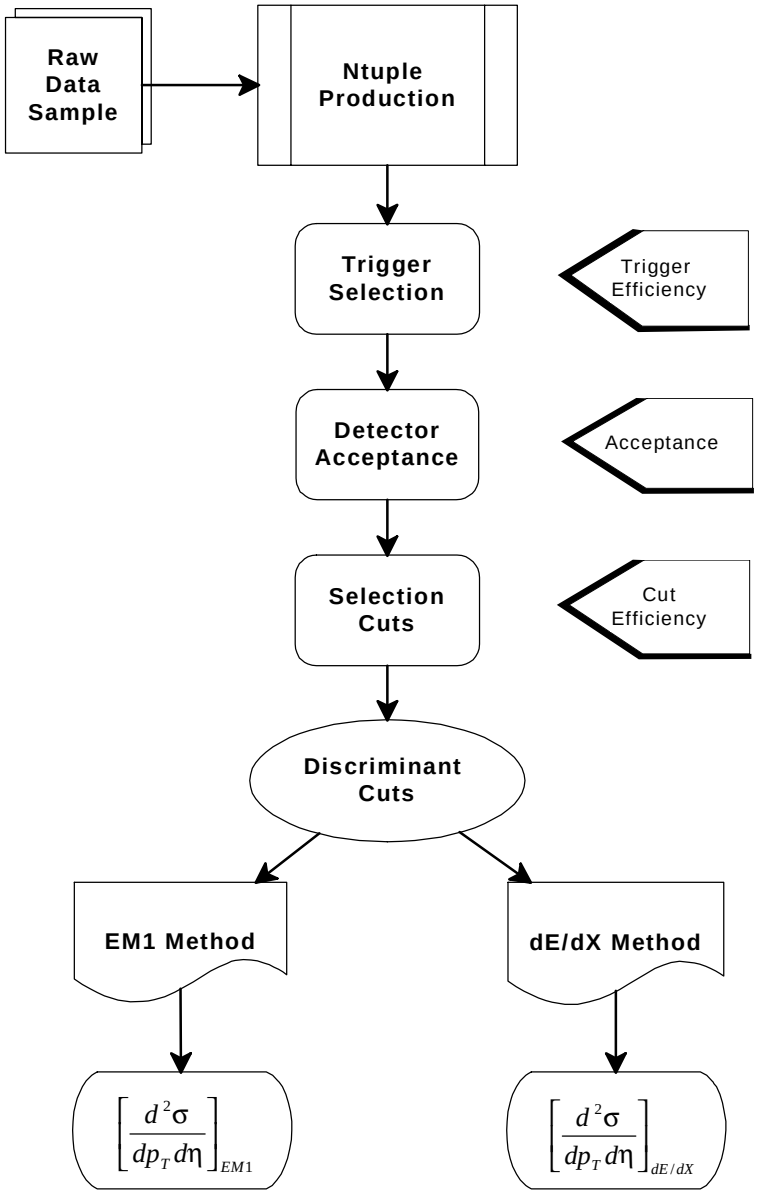

Figure 4.1: Flow chart of direct photon analysis procedures.

before reaching the tracking detectors. For cross section calculations, we restrict the search to the highest E_T , isolated photon candidates where background signals are expected to be reduced.

A typical event display generated by the DØ PIXIE package [23] for a RUN 1A event with a photon candidate which passed our standard trigger and off-line cuts is given in figure 4.2. The photon EM calorimeter cluster and the accompanying jet are shown in the combined tracking plus calorimeter display. To further understand the photon's behavior, an energy deposition profile within the 4 EM layers of the End Calorimeter is shown in figure 4.3.

The geometrical structure of a typical photon event contains one or more jets on the opposite side in azimuth. Our event sample also contains a small fraction of di-photon events. Figure 4.4 shows the azimuthal angle separation between the photon and jet which is peaked at 180 degrees or a back-to-back orientation.

4.3 Triggering on Photons

The forward direct photon candidates materialize as electromagnetic showers in the End Calorimeter. To trigger on these candidates, we mainly used a two-level scheme utilizing the trigger towers in the ECEM. Photons are copiously produced with a cross section much larger than most rare physics events like W and Z at the $p\overline{p}$ collider. In order not to overwhelm the data-taking bandwidth of the DØ Data Acquisition system, events with the photon triggers have to be properly *pre-scaled* with a set of pre-determined factors. Since the photon cross section drops quickly with increasing E_T , the trigger is separated into several E_T regions. To collect data in the lowest E_T range, dedicated special runs were taken that emphasized these high rate regions.

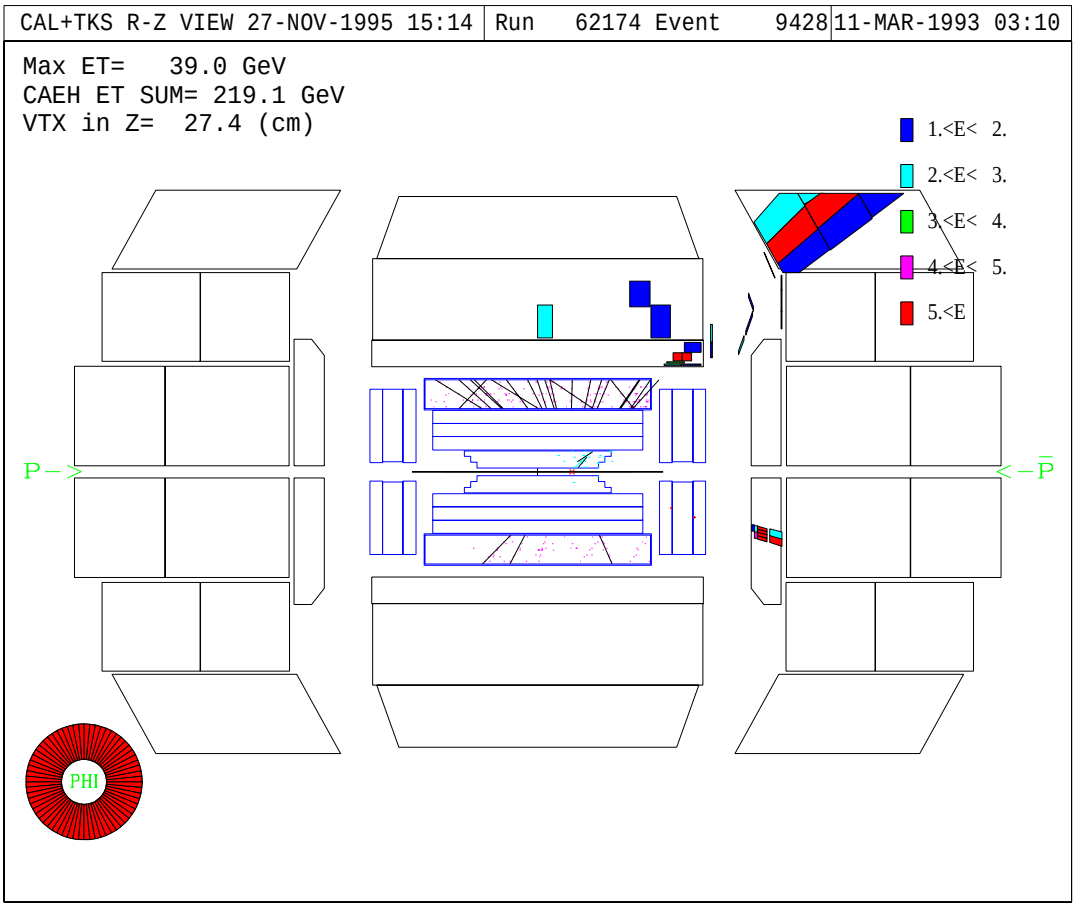

Figure 4.2: A typical photon event display for 1A run number 62174, event 9428. The photon candidate has an E_T of 58.7 GeV and is located in the forward region at $\eta = 1.84$, where it can be seen as the cluster of energy in the ECEM on the lower right hand side.

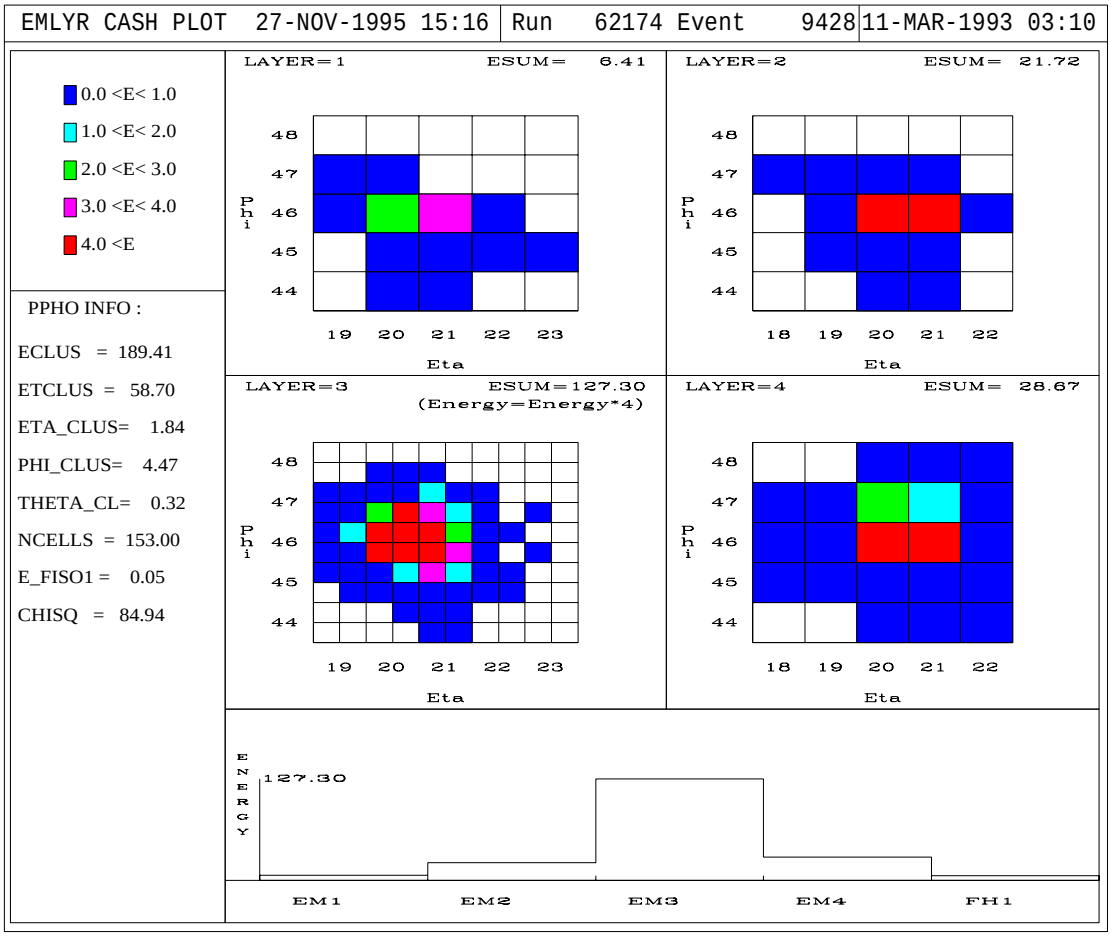

Figure 4.3: EM End Calorimeter energy deposition is shown in profile for the 4 longitudinal layers for the photon candidate of figure 4.2. The finer segmentation and maximum energy deposition can be seen in layer 3.

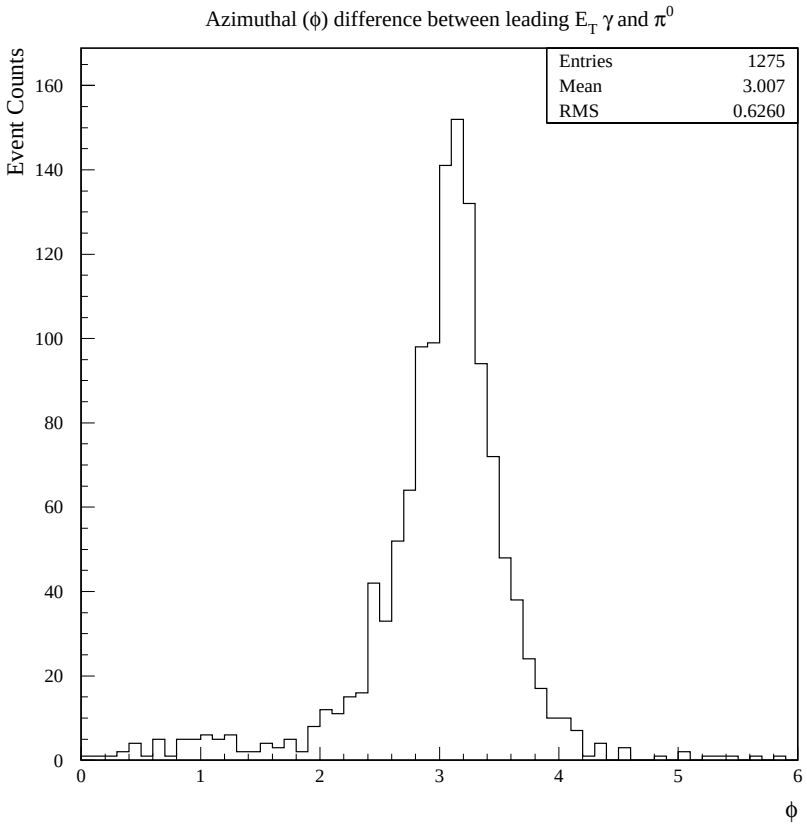

Figure 4.4: The azimuthal separation of the leading E_T photon and jet shows that they are virtually back-to-back. The photons passed all off-line selection cuts and the events are required to have only one jet.

4.3.1 Level-1

Level-1 is a hardware trigger system which makes fast analog sums of Electromagnetic Calorimeter energies in towers of 0.2×0.2 in (η, ϕ) space. We required that one or more electromagnetic trigger towers have their E_T values greater than certain thresholds to qualify as good EM candidates. The Level-1 trigger thresholds used for the three major photon E_T regions are, separately, 2.5, 7, and 10 GeV. There correspond Level-2 software filters which have comparable energy thresholds.

4.3.2 Level-2

Level-2 is a software filtering system that groups calorimeter cells with a clustering algorithm and requires that the energy deposition patterns be consistent with electron test beam data samples. The criteria for passing the Level-2 photon filter are that the candidates had to have one or more electromagnetic clusters with E_T values greater than one of the three threshold values, 6, 14, and 30 GeV. Once the candidate passed the Level-2 criteria, the filter software then sets the corresponding filter bits and also store these in the data. The candidate clusters were also required to have shapes consistent with photons and to pass an on-line isolation cut.

Further classification of the photon data was done by organizing the photon samples into three main E_T regions corresponding to the following off-line cuts,

1. 10 – 22 GeV (LOW)
2. 22 – 34 GeV (MEDIUM)
3. 34 – 100 GeV (HIGH)

These E_T regions are chosen such that the trigger/filter efficiencies are essentially close to 100% over the E_T regions covered. This was indicated by earlier trigger studies [24]. Another check for the photon trigger/filter efficiencies was done by

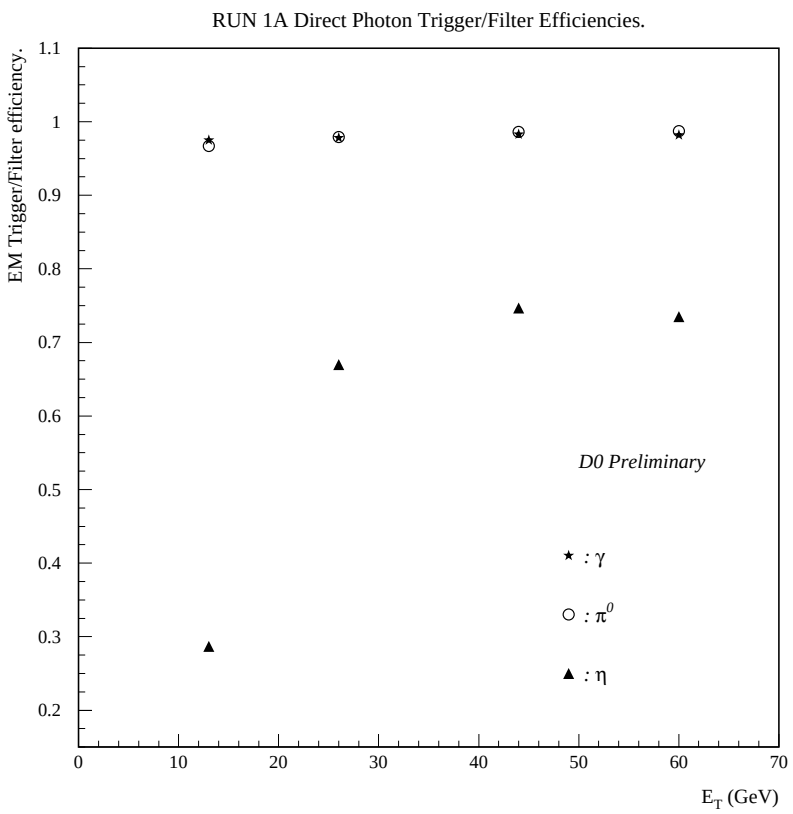

Figure 4.5: Direct photon trigger/filter efficiencies as determined by trigger simulations.

using Monte Carlo photon samples and the D0 Trigger simulator framework with exactly the same trigger/filter configuration used in taking the data. The results showed that the photon triggers were indeed close to 100% efficient as can be seen in figure 4.5 for photons and π^0's.

4.3.3 Trigger/Filter Coverage for Run 1A

For the three main trigger/filters used in RUN 1A, we have studied the trigger coverage as a distribution in pseudorapidity. Figure 4.6 is an example of the pseudorapidity distribution taken with the low E_T trigger during special runs with dedicated photon triggers. During these runs the central region $-1 < \eta < 1$ was slightly suppressed

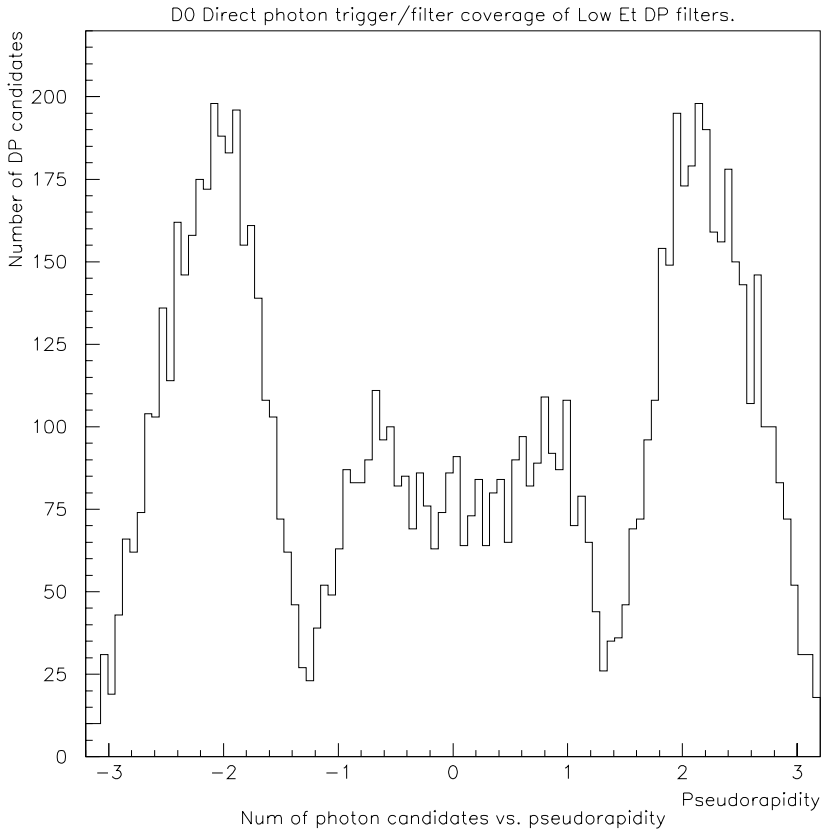

Figure 4.6: The pseudorapidity coverage of the DØ direct photon low E_T trigger/filters, taken during dedicated special runs.

compared to the forward triggers, and in the figure the dips around $\eta = 1.4$ and $\eta = -1.4$ are due to the geometrical inefficiency at the gap between the central and end calorimeters. This plot shows that DØ has photons copiously produced in the forward pseudorapidity region.

4.3.4 Estimation of Integrated Luminosity

To calculate the direct photon cross section, one needs to estimate the total luminosities corresponding to the three major photon trigger/filters. The integrated luminosities are estimated by the DØ Production Database query tools [25]. In the following table the Level-2 names and E_T thresholds for the filters are summarized,

as well as the estimated integrated luminosities and number of events collected with the corresponding filters. The values are then used in the cross section calculation.

Table 4.1: Forward photon trigger/filters and corresponding integrated luminosities.

Triggers/Filters			
Level-2	E_T threshold (GeV)	$\int dt(pb^-1)$	Number of Events
GAM_LOW_ISO	6	0.0124	127,270
GAM_MED_ISO	14	0.1297	91,184
GAM_HIGH_ISO	30	12.770	378,460

4.4 Backgrounds

Major sources of backgrounds to the direct photon signal come from decay processes of the π^0 and η mesons. These mesons themselves are copiously produced as fragmentation products of final state partons and they immediately decay via the following processes [26],

$$\pi^0 \rightarrow \gamma + \gamma \quad (BR = 98.798\%) \tag{4.1}$$

$$\eta \rightarrow \gamma + \gamma \quad (BR = 38.8\%) \tag{4.2}$$

$$\eta \rightarrow \pi^0 + \pi^0 + \pi^0 \quad (BR = 31.9\%) \tag{4.3}$$

The contributions from these background decay processes greatly complicated the analysis. With the detector resolution, these background events cannot be fully reconstructed on an event-by-event basis. Instead, the analysis methods described here use the different conversion probabilities between the various particle types as a method to separate them statistically.

4.5 Conversions within the Detectors

The major background particles, the isolated π^0's and η's, both decay within the detector volume before entering the forward drift chamber and End Calorimeter. The decay products are photon pairs which may appear as coalesced photons within our spatial resolution in the End Calorimeter.

The situation is complicated by the amount of material before the detector which allows some photons to convert into e^+e^- pairs (the details of the conversion will be given later). The coalesced photon pairs from neutral meson decays have a high probability to show up as merged tracks of converted electrons. The real signal we are looking for, the direct photons, also suffers the same conversion probability. Therefore, we cannot limit the photon candidate data sample to just the candidates without tracks. Instead, we must account for all possible candidates in the detector, and do not use the criteria of *with track* or *without track* to tag candidates as either photons or electrons.

4.5.1 Decay and Conversion Schemes

To understand the underlying background particle contributions, we use the neutral π^0 decay as an example for describing the decay and conversion schemes. The angular separation between the two photons from the π^0 decay depends on the momentum of the parent π^0. If the π^0 has a very small E_T , it is possible that the two decay photons will have a large opening angle between them, and only one photon lies within

the (η,ϕ) cone area used by the DØ Electron ID algorithms [27] for EM candidate detection. As the π^0 E_T gets higher, the two photons coalesce and both will be detected within the same cone by the algorithm.

For single photons, the energy loss in the detector is mainly from electron/positron pair production. Within the detector material, the energetic pair-produced electrons and positrons then go through bremsstrahlung processes and further radiate more photons. This cascading effect is what is used in the electromagnetic calorimeters to detect particle showers and forms the main technique for photon identification.

4.5.2 Conversion Probability Estimation

To estimate the photon conversion probability at a particular detector depth, we utilize the fact that the probability for a photon to travel a distance X without a pair-production interaction is given by [28]

$$e^{-X/\lambda_{pair}}. \tag{4.4}$$

Here λ_{pair} is the mean free path of the photon for pair-production, which can be related to the radiation length (the distance over which an electron loses $\frac{1}{e}$ of its energy by radiation loss alone) [28],

$$\lambda_{pair} = \frac{9}{7} L_{rad} \tag{4.5}$$

Therefore, the photon conversion probability due to pair-production within the detector after a distance X can be estimated by summing the materials present, in units of the corresponding radiation lengths, and substituting the results into the conversion probability formula.

$$P_{conversion} = 1 - e^{-\frac{7X}{9L_{rad}}} \tag{4.6}$$

The amount of material in front of the Forward Drift Chamber was measured during the detector construction period. All materials were carefully weighed and their contributions to the total radiation length at various pseudorapidity or detector depths were estimated and incorporated in the detector simulation Monte Carlo package, D0GEANT. We therefore could just use D0GEANT to summarize the amount of detector material and estimate the corresponding conversion probabilities at the different pseudorapidity ranges, as summarized in figure [4.7].

The conversion probabilities are fairly flat except in the region of the ICD where the amount of material is high. We restrict our study to the region where the conversion probabilities are relatively flat, $1.6 < |\eta| < 2.5$. The average amount of material in this region is 0.62 ± 0.09 radiation lengths, which corresponds to a conversion probability of $38\% \pm 4\%$.

As a consistency check we used Monte Carlo generated photon data and the D0GEANT program to measure the photon conversion probability and the results are given in table 4.2. These probabilities have to be corrected for the tracking inefficiency by the relation,

$$Conversion\_Fraction = P \times T \tag{4.7}$$

where P is the conversion probability and T is the tracking efficiency. The tracking efficiency is estimated independently. A set of Monte Carlo single electrons are generated for this purpose, and at an E_T of 44 GeV, the tracking efficiency is estimated to be 0.9741. This gives a conversion probability of 0.378, which agrees with what we obtained from the average radiation length calculations. Therefore, the conversion probabilities estimated by the D0GEANT program do provide a consistent description of the detector material for the pseudorapidity region being considered in this analysis.

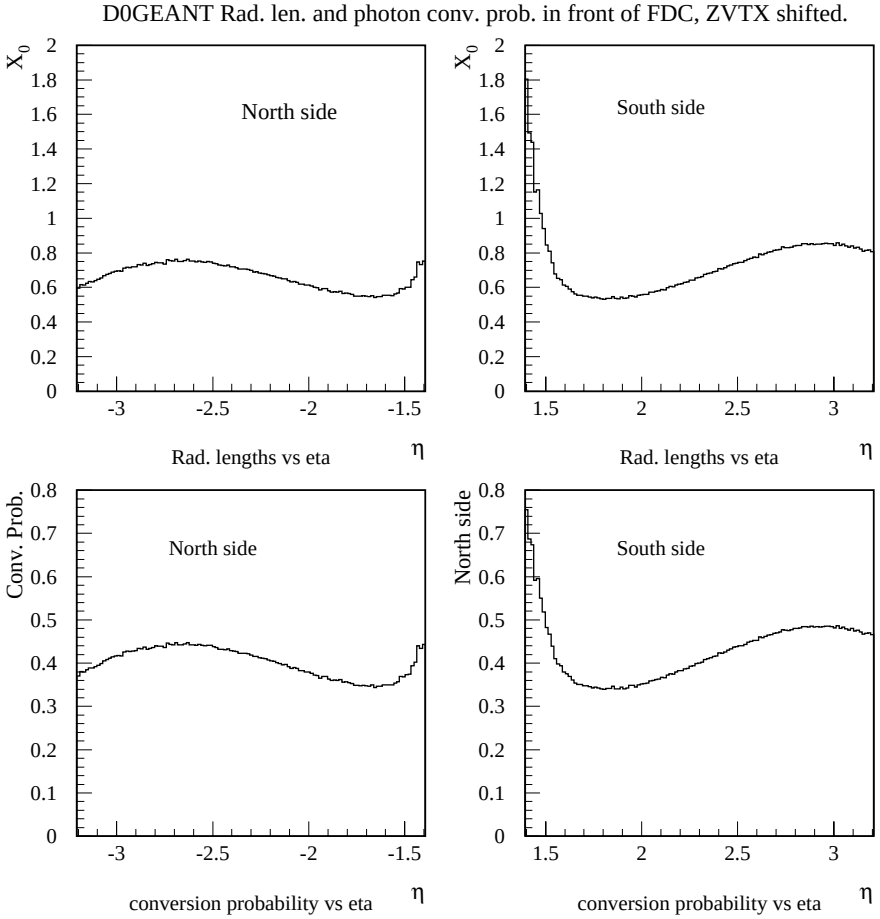

Figure 4.7: Radiation lengths and conversion probabilities versus pseudorapidity. The asymmetry in η is due to the Z vertex shift from the detector center during RUN 1A.

Table 4.2: Forward photon conversion probabilities before the FDC, as indicated by the Monte Carlo photon samples.

Photon Conversion Probabilities				
E_T (GeV)	Accepted	Converted	Conversion Probability	C.P. Error
13	3656	1286	0.3515	0.0079
26	3523	1273	0.3613	0.0081
44	2374	874	0.3682	0.0099
60	2403	895	0.3725	0.0099
100	1380	486	0.3522	0.0129

4.6 Monte Carlo Event Generation

It is clear that one needs to study the detector responses to various types of particles. Where there is no experimental data we use Monte Carlo generated data to mimic the real data as close as possible. Pythia and Isajet Monte Carlo programs were used to generate single photons, π^0's, and η's. These simulated data were then passed through the D0GEANT program, using a full *plate* level configuration which has a detailed description of the calorimeter geometry and material. The output of the simulations then go through the same version of the reconstruction programs to ensure self-consistency. To simulate realistic data we add contributions from the underlying events and pile-up by superimposing minimum bias collider data with the Monte Carlo events.

Since the background to the direct photon data sample is mainly π^0 and η mesons, we made a sample of mostly background events by adding the Monte Carlo simulated π^0 and η sample together. This background-like sample is used by the analysis methods described in the next chapter.

Chapter 5

Analysis Strategies

5.1 Event Selection

The Direct Photon data for DØ RUN 1A were mainly from the following categories,

1. Special runs with specific photon triggers, and
2. General collider physics runs which had the photon triggers extracted and put onto the QGA data set.

The data went through reconstruction and a series of DST analyses and ntupling. The resulting ntuple files are the main data set on which the fine-tuning of off-line selection cuts began. After the trigger/filter selections from the original data samples, the following off-line selection cuts were applied to reduced the backgrounds :

1. $1.6 < |\eta_{physics}| < 2.5$
2. $16 < |\eta_{detector}| < 25$
3. $|Z_{VTX}| < 50cm$
4. $E_T(R = 0.4) - E_T(R = 0.2) < 2GeV$

5. $EMFraction > 0.96$

6. $\chi^2 < 150$

7. $E_T(missing) < 20$

8. $Track\_Match\_Significance < 5$

Cuts 1, 2, and 3 restrict the fiducial region of the detector to where the photon conversion probability is fairly uniform. Cut 4 reduces the contribution from the anomalous photon processes. Cut 5 ensures that the photon candidates selected have mainly electromagnetic energy and almost no hadronic activity in the calorimeter. Cut 6 utilizes the calorimeter *H-matrix* effective chi-square value obtained by including various calorimeter variables in the covariance matrix construction. Test beam and Monte Carlo data were used in this algorithm to provide χ^2 values consistent with clean electron or photon data samples. Previous studies indicated that a cut of χ^2 at 150 will ensure the quality of the EM candidates. The same cut was used for the central region analysis, so a comparison between central and forward results will be possible. Cut 7 blocks events which have photon/electron candidates principally from W boson decays. Cut 8 ensures that for candidates with matching tracks in the same calorimeter (η, ϕ) space the association is reasonably good.

As a reference set of well defined electron candidates, we have studied W and Z vector bosons and their decays into electrons [29, 30]. The cuts are selected to have high efficiencies in identifying the electrons from W or Z decays. In addition, the following selection criteria were applied to the Z sample to ensure a clean data sample.

- for the two highest E_T candidates : $E_T > 25$ GeV (each)
- for the highest E_T candidate : $1.6 < |\eta\ | < 2.5$

The invariant mass distribution of the two highest E_T EM candidates is shown in figure 5.1 for the Z sample just described. A Z mass peak is seen on top of

some background which mainly consists of QCD di-jet events (where the jets faked electrons) and Drell-Yan processes which also produce electron and positron pairs just like the real Z events [30]. A multiple Gaussian fit to the data was performed. The data is then split into a Z signal region which is within ± 2 standard deviation of the Z mass peak and and into a background region. Using the fit it is estimated that the purity of the Z sample is 60% in the signal region. We apply the the standard direct photon cuts to the EM candidates from the Z sample in the two regions and compare their relative effectiveness.

The most controversial of the photon cuts is the isolation cut. An issue in the analysis was whether to use either an absolute value cut on energy (E) or transverse energy (E_T) in the isolation region, which is the angular ring-shaped region between radii 0.2 and 0.4 from the EM shower center in (η,ϕ) space. An energy fraction cut was ruled out since the background contribution in the isolation area energy is not likely to increase as we go to higher photon candidate E_T. The relative merits of the E and E_T cuts were compared by applying both of these cuts to the EM candidates from the Z sample, and calculating their respective efficiencies. The efficiency study is summarized in table 5.1, in which 4 of the most important cuts are listed for the region in the invariant mass distribution consistent with signals and the region consistent with backgrounds. (The background contribution to the signal region is not subtracted from the signal region efficiency as this is simply a check for the relative efficiencies.) Here we apply the cuts in various combinations and study the optimized set of cuts which passes the EM candidates efficiently.

To further emphasize the fact that the total isolation energy cut is too strict, we present a 2-dimensional scatter plot in figure 5.2 which shows the distribution

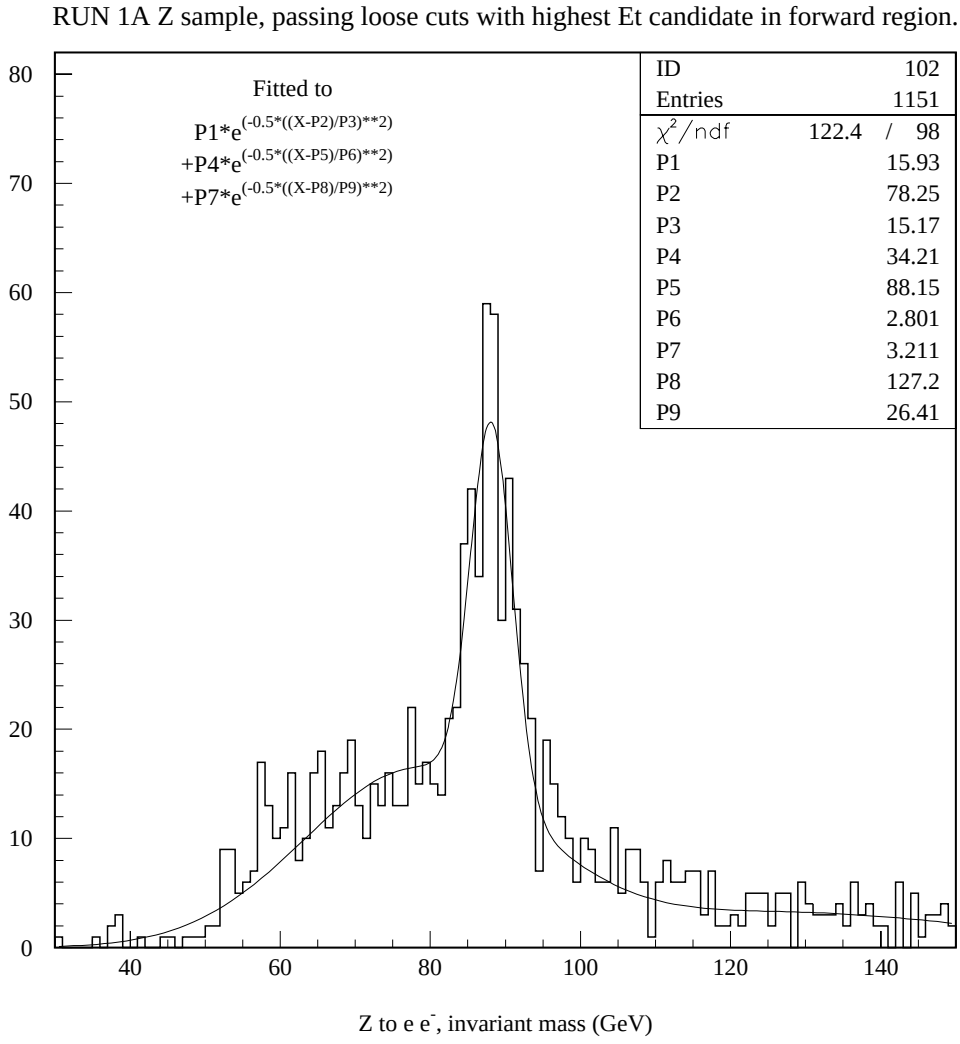

Figure 5.1: Invariant mass distribution from the two leading E_T EM candidates from the Z sample. The region within 2 standard deviations from the fitted peak is used to study the relative efficiencies of the selection cuts on an enhanced signal sample. The regions outside of this are used to study the backgrounds.

Table 5.1: Forward Photon Efficiencies as obtained from the Z sample.

Cut Efficiency Estimation		
Cuts applied	candidates consistent with Z electrons	candidates consistent with backgrounds
cut_1 ($E_T(R=0.4) - E_T(R=0.2) < 2GeV$)	81.77%	57.99%
cut_2 ($E(R=0.4) - E(R=0.2) < 5GeV$)	62.81%	37.45%
cut_3 ($\chi^2 < 200$)	84.73%	58.39%
cut_4 ($EMFraction > 0.96$)	94.83%	89.53%
cut_1,3	74.88%	43.62%
cut_1,4	79.06%	53.15%
cut_3,4	83.25%	55.70%
cut_1,3,4	74.14%	41.88%
cut_2,3	58.13%	30.34%
cut_2,4	61.58%	34.90%
cut_3,4	83.25%	55.70%
cut_2,3,4	58.13%	29.26%

of isolation area E_T versus E. A maximum E cut at 2 GeV is too stringent and will eliminate too many good EM candidates from the Z samples. If we raise the maximum E cut to 10 GeV, most of the eliminated candidates will be removed by a maximum E_T cut at 2 GeV anyway.

The isolation cut is investigated further by using Monte Carlo photons to study the efficiency at higher E_T values. For a cut at 2 GeV the efficiency starts to decline at E_T of 60 GeV, and has dropped to around 76% at 100 GeV. Initially it was felt that the drop in efficiency is due to the EM fraction cut. Monte Carlo studies showed that the loss is due to the fixed maximum value of 2 GeV for the isolation area E_T. By raising the maximum E_T cut value, the efficiency remains relatively flat. This effect can be seen in figure 5.3).

This drop in efficiency indicates that as E_T rises, even clean photon candidates start to deposit a larger amount of energy in the isolation area. We are left with two options, either change to a looser isolation cut value (for flat efficiency), or use the 2 GeV cut value as it is. We have chosen the latter option with the reduced efficiency at high E_T since that is how the isolation cut is implemented in the theoretical QCD calculation. The efficiency of the maximum 2 GeV isolation cut can be checked with the leading E_T EM candidates in the Z sample. The candidates have E_T of approximately 40 GeV. This cut removes about 10% of the distribution shown in figure 5.4.

Since the cut efficiencies are E_T dependent, a method had to be adopted to study this dependence. The Z and W boson sub-samples are limited to E_T values around 40 GeV and hence are limited for our purpose of studying the E_T dependence. Instead we use Monte Carlo photons at discrete E_T's and extract the standard photon cut efficiencies from each of these E_T regions. No scaling was applied to the Monte Carlo cut efficiencies. The detector acceptance and combined cut efficiencies are listed in the following table and are plotted in figure 5.5.

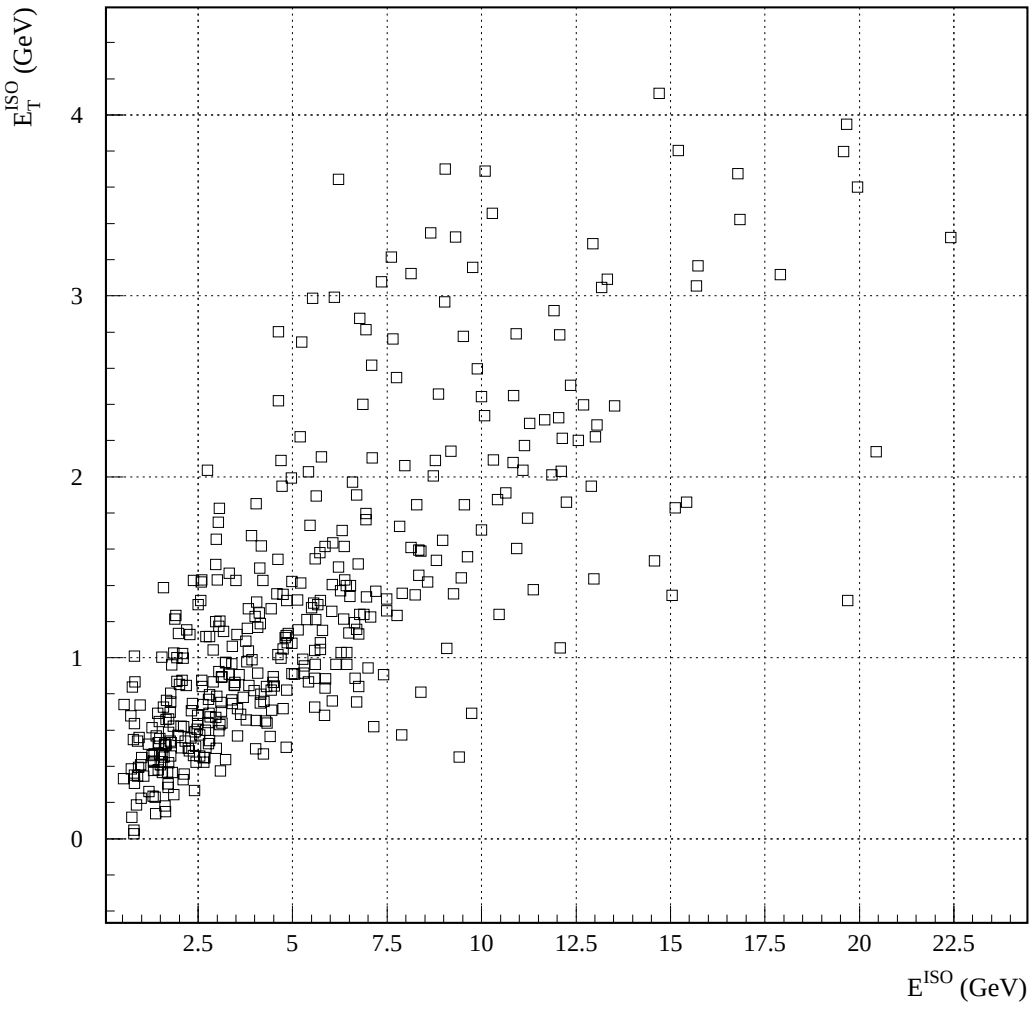

Figure 5.2: Isolation area E_T versus isolation area E distribution for the leading E_T EM candidates in the forward region from the Z sample.

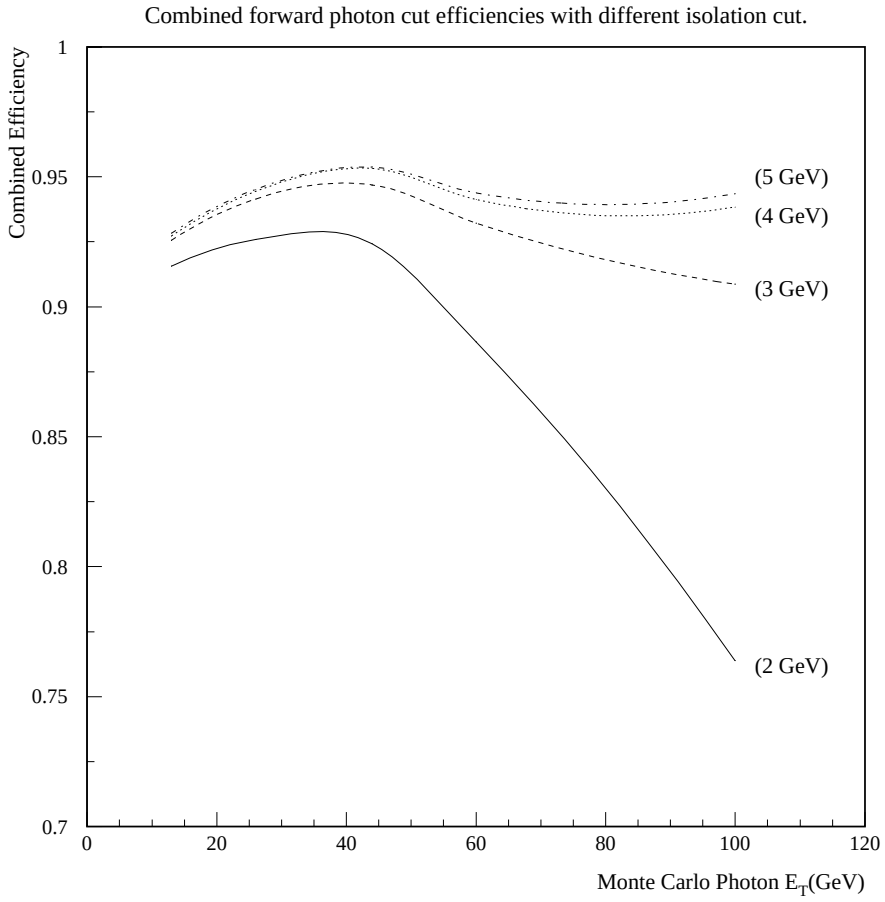

Figure 5.3: Combined cut efficiency of the three major photon cuts – isolation, EM energy fraction, and χ^2 as applied to Monte Carlo single photons with increasingly higher p_T. The various curves indicate different isolation cut values, from 2 GeV for the solid line at the bottom to 5 GeV for the dash-dotted line at the top.

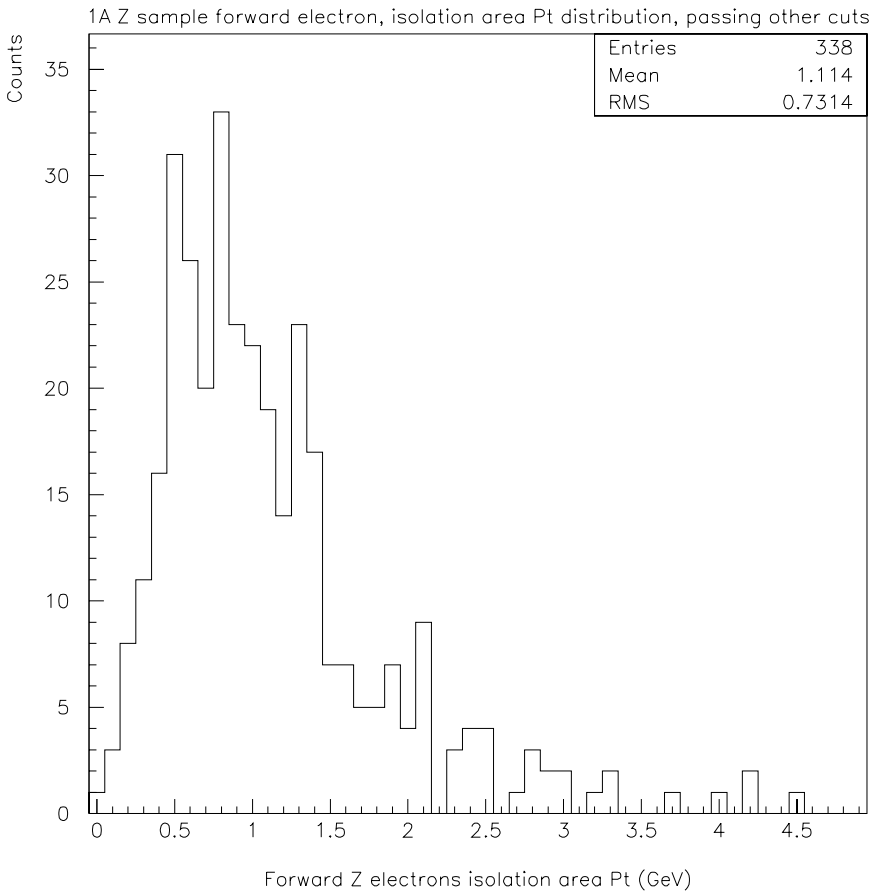

Figure 5.4: Isolation area E_T distribution for the leading E_T EM candidates from the Z sample.

Table 5.2: Forward photon detector acceptance and selection efficiencies as indicated by the Monte Carlo photon samples.

Acceptance and Cut Efficiencies				
E_T (GeV)	Acceptance	Error	Cut Efficiency	Error
13	0.916	0.004	0.842	0.006
26	0.913	0.005	0.854	0.006
44	0.932	0.005	0.852	0.007
60	0.919	0.005	0.816	0.007
100	0.923	0.007	0.718	0.012

With the EM layer 1 method of background estimation, we restrict the data sample to events without any tracks associated with the EM showers. As a result, a separate track association cut efficiency has to be estimated and included in the cross section calculation. This is again done with the Monte Carlo photon sample. Since we require photon candidates not to be associated with tracks, this efficiency is one minus the probability for a photon to convert and be detected as a track. Additional terms have to be included to account for the possibility of charged or neutral (which then decays and appears as charged) meson overlaps.

$$\epsilon_{trackassociation} = 1 - PT - U(1 - P^2) \tag{5.1}$$

where U is the overlap probability, which can be estimated from the W, Z data samples [31]. The efficiencies thus obtained at each E_T point are shown in figure 5.6.

The overlap probability U can be measured from the W, Z data samples, but this is limited to E_T values around 40 GeV. We estimated the E_T dependence of the combined selection and track association cut efficiency only by the Monte Carlo

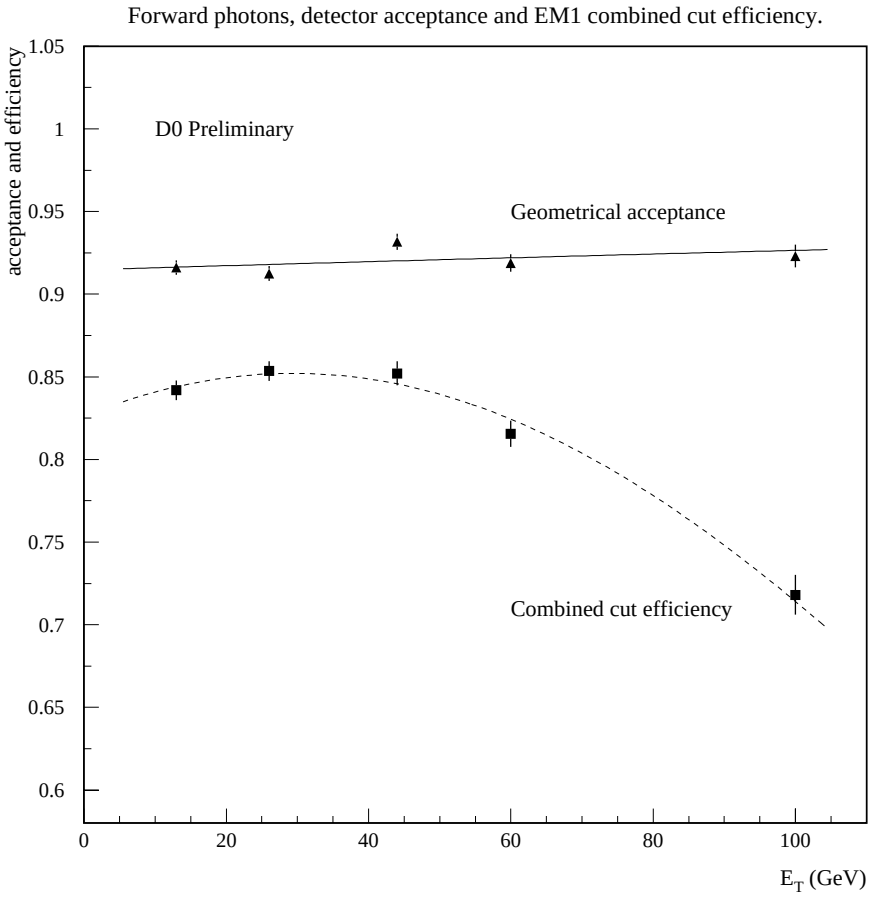

Figure 5.5: Photon detector acceptance and combined cut efficiency versus E_T. The decrease in the efficiency at higher E_T is due to the isolation cut criteria.

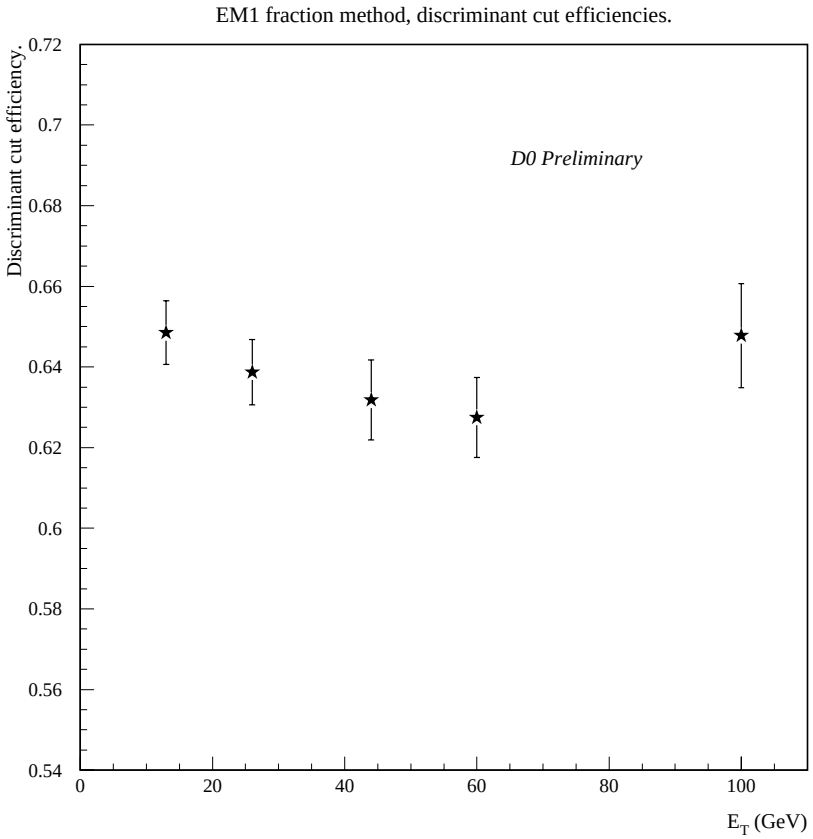

Figure 5.6: The effect of the track association cut for the EM1 method on the efficiency.

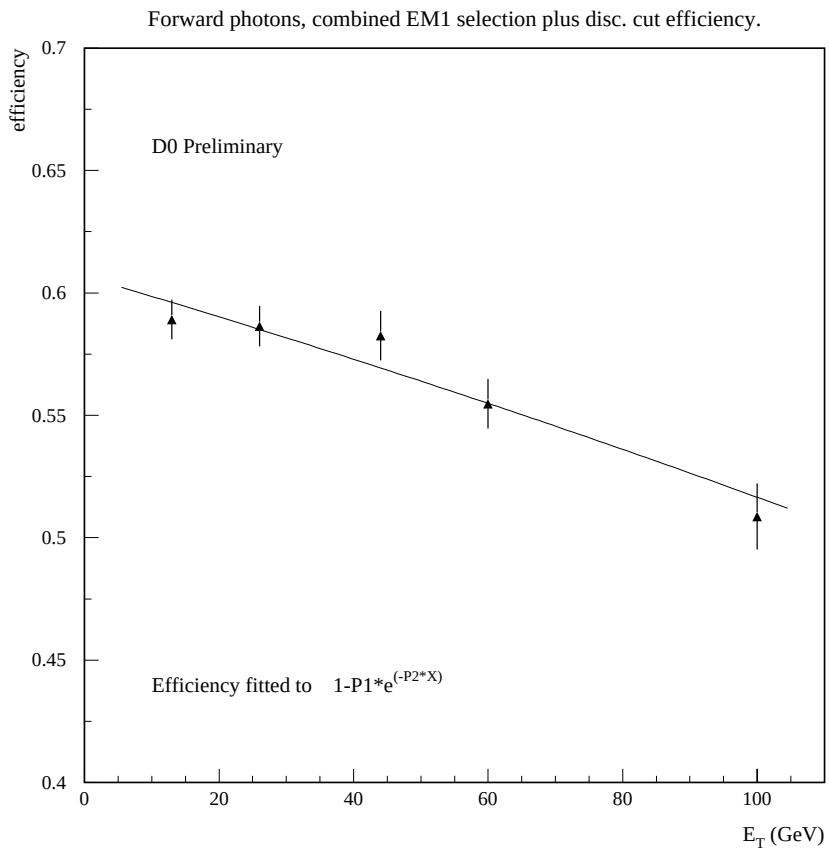

Figure 5.7: The photon detection efficiency after combining the EM1 track association cut with the standard photon selection cuts.

photons. The resulting combined efficiencies are shown in figure 5.7. These are the efficiency values used in the cross section calculation.

5.2 Methods of Background Estimation

The DØ direct photon data sample has a large contribution from the underlying neutral π^0 and η mesons which decay rapidly into di-photon pairs. For example, a

photon candidate with an E_T of 60 GeV and a pseudorapidity of 2 has a 30% chance of being a real direct photon. Due to the lack of a magnetic field in the tracking volume, the electrons and positrons from the converted photons are almost always detected as a single track. Since direct photons also have a high probability (about 38%) of converting inside the detector, an event-by-event discrimination between real direct photons and photons from neutral meson decays is impossible.

We used two analysis methods to statistically measure the relative contributions from direct photons and background particles. These two methods are

1. EM1 Fraction Method, using the first layer of the End Calorimeter, and
2. dE/dX Method, using the Forward Drift Chamber.

Both of the above methods are manifestations of the so-called *conversion method*, since they both utilize the differences in the rate of conversions in the detector as a basis for statistical separation.

5.2.1 Discriminators

For all variants of the general conversion method, the extraction of the relative fractions of photons and background contributions can be illustrated by the following scheme. We find a set of detector variables that depend mostly on the relative conversion probabilities of the photon and background events, and from these variables we then define the track association cut efficiencies for various particle types. For example, if ϵ, ϵ_γ, and ϵ_π are separately the track association cut efficiencies for data, photons, and backgrounds (the latter two categories can be simulated with Monte Carlo), and γ is the fraction of real direct photons (which is called *photon purity* in this analysis), then the following relationship holds :

$$\begin{pmatrix} 1-\epsilon \\ e \end{pmatrix} = \begin{pmatrix} 1-\epsilon_\gamma & 1-\epsilon_\pi \\ \epsilon_\gamma & \epsilon_\pi \end{pmatrix} \begin{pmatrix} \gamma \\ 1-\gamma \end{pmatrix} \tag{5.2}$$

By solving for γ we obtain the definition of the the fraction, or purity of photons among all particles in our final data sample,

$$\gamma = \frac{\epsilon_\pi - \epsilon}{\epsilon_\pi - \epsilon_\gamma} \tag{5.3}$$

The corresponding statistical and systematic error are given by the following relationships,

$$\delta\gamma\,(statistical) = \frac{\delta\epsilon}{\epsilon_\pi - \epsilon_\gamma} \tag{5.4}$$

where $\delta\epsilon = \sqrt{\epsilon\,(1-\epsilon)\,/N}$

$$\delta\gamma\,(systematic) = \frac{\epsilon_\pi - \epsilon}{(\epsilon_\pi - \epsilon_\gamma)^2}\delta\epsilon_\gamma + \frac{\epsilon - \epsilon_\gamma}{(\epsilon_\pi - \epsilon_\gamma)^2}\delta\epsilon_\pi \tag{5.5}$$

where $\delta\epsilon_\gamma$ and $\delta\epsilon_\pi$ are separately the errors corresponding to the efficiencies for photons and backgrounds.

We will elaborate further on the details of the two main methods used for the photon purity extractions.

5.3 Electromagnetic Shower Profile Method

Traditionally physicists have used the different shapes in electromagnetic shower development between photons and background particles like π^0's to separate them statistically [32]. The shower shapes can vary transversely or longitudinally relative to the particle direction as the electromagnetic showers develop within the calorimeters. Earlier DØ studies using Monte Carlo photon and π^0 samples demonstrated that it is very difficult to use the differences in transverse shower shapes to separate photons and π^0 s [33]. In the analysis of DØ RUN 1A direct photon data we use the longitudinal shower development profile as a way to extract the ratio of direct photons from the backgrounds.

5.3.1 EM Layer 1 Energy Deposition as a Discriminator

Table 5.3 lists the number of radiation lengths of material in each of the 4 layers in the End Calorimeter. Purely electromagnetic showers will be contained in these 4 layer, and have their shower maximum located in layer 3 where the cells are more finely segmented.

Table 5.3: Radiation lengths in the 4 readout sections of End Electromagnetic Calorimeter.

ECEM	
ECEM Layer	Radiation Length (X_0)
Layer_1	0.3
Layer_2	2.6
Layer_3	7.9
Layer_4	9.3

π^0's and η's, which form the main backgrounds, decay into two photons. These photon pairs will most likely convert in the cryostat wall or the first few absorber plates in the first EM layer (EM1). Since π^0's and η's have two photons, it is more likely that they will deposit more energy in EM1 than a single photon will. We use the fraction of energy deposition in EM1 as a technique to distinguish single direct photons from backgrounds.

The EM1 energy longitudinal deposition profile is shown in figure 5.8 as a fraction of the EM1 layer energy to the total energy. Both Monte Carlo single photons and π^0's were generated at fixed E_T's, and their EM1 fractions are shown. The major background, π^0's, leave more energy in the first EM layer than single photons.

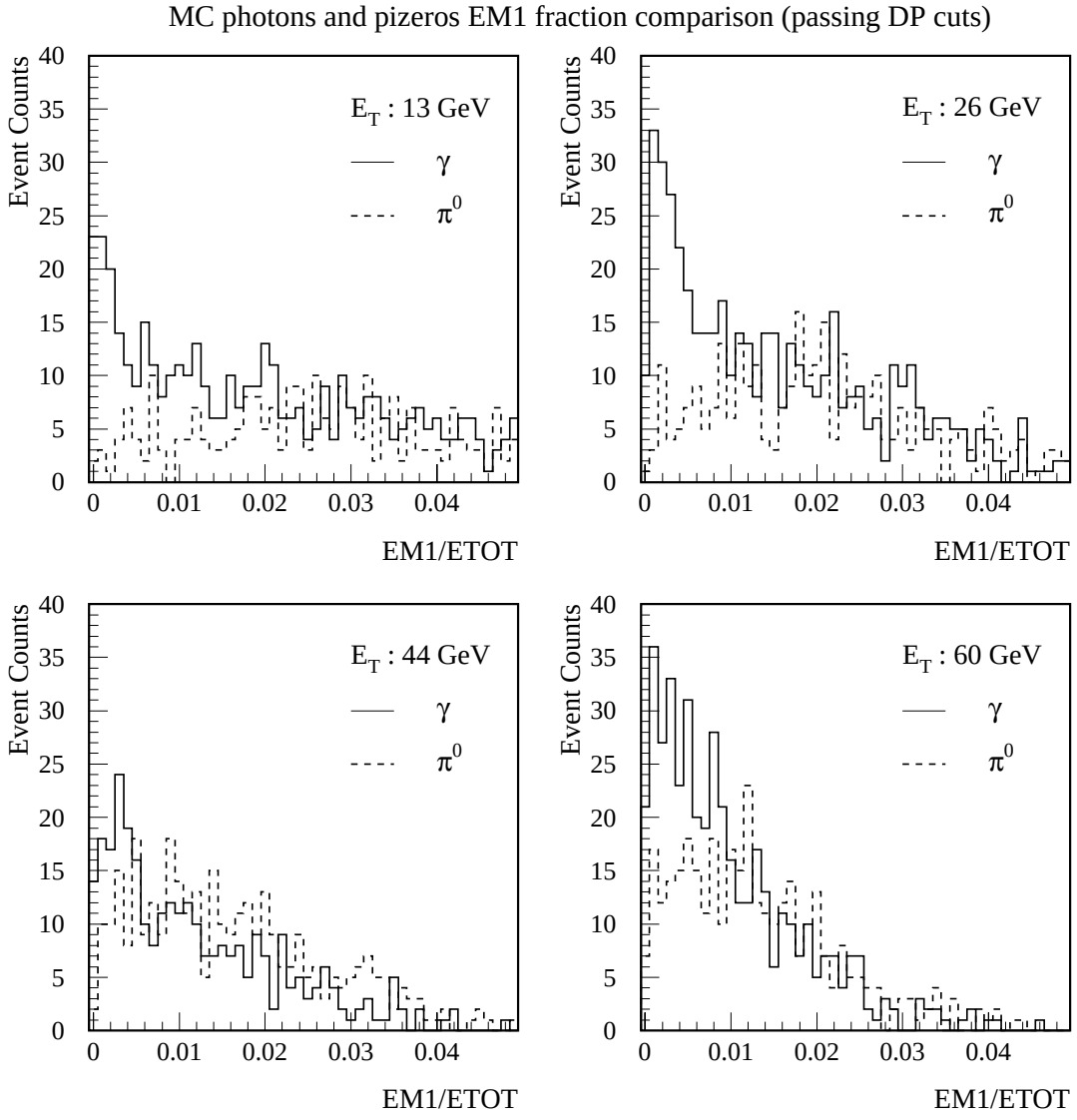

Figure 5.8: Comparison of Monte Carlo photon and π^0 EM1 energy deposition fractions.

5.3.2 Extraction of Photon Purities with the Fitting Method

The D0GEANT detector Monte Carlo was used for detector simulation to provide the number of radiation lengths and conversion probabilities for the pseudorapidity region studied. With the aid of Monte Carlo physics events generated by ISAJET and PYTHIA as described in the previous chapter, we were able to study the detector acceptance and cut efficiencies which are both required for cross section calculations.

A detailed distributions of quantities like the EM1 layer energy deposition fraction revealed some shifts in the absolute scale of Monte Carlo simulated data with collider data. This difference shows up mainly at higher values of EM1 energy fractions. This produces an uncertainty in the derived photon purity. It is encouraging that the shapes of the Monte Carlo simulated data are similar to the real data, especially in the low EM1 energy fraction region where the difference between photons and π^0's is larger. There are two methods to study this effect,

1. Derive the scale differences between Monte Carlo and the W data sample, and use this factor to scale the Monte Carlo distributions.

2. Make further cuts on the EM1 fraction to reduce the scale dependence.

When an absolute value cut on $EM1/ETOT = 0.01$ is made, the photon purity as defined in equation 5.3 is negative which is unphysical. This is due to the differences between the data and the Monte Carlo at high $EM1/ETOT$ values. The data has more contamination than is simulated in the Monte Carlo. The contamination shows up as more energy in EM1 than is predicted by the Monte Carlo. To reduce the contamination we focus on the $EM1/ETOT$ region where photons and neutral mesons behave differently, namely the low $EM1/ETOT$ region. Using the logarithm (base 10) of the $EM1/ETOT$ ratios, we make a distribution out of these transformed values. The resulting distribution focuses more on the low $EM1/ETOT$ region and thus provides a better discriminating patterns for separation between photons and

backgrounds. Constrained χ^2 fits [34, 35] were then carried out to fit the Monte Carlo distributions to the data distributions at each E_T point, with the relative particle fractions as the fitted parameters. In this way, we obtained a set of reasonable relative particle fractions.

This fitting is done by assuming that the $\log(EM1/ETOT)$ distribution of data is a superposition of the various contributing distributions convoluted with their respective fractions,

$$F_j = f_\gamma B_j^\gamma + f_{\pi^0} B_j^{\pi^0} + f_\eta B_j^\eta \tag{5.6}$$

where the F_j's and B_j's are the $\log(EM1/ETOT)$ values of the data and Monte Carlos at the E_T bins, and the fractions are constrained, $0 < f_i < 1$, and normalized, $\sum f_i = 1$.

To actually perform the fitting with the above constraints, the following relations are used [36],

$$\begin{aligned} f_\gamma &= P_2 && (5.7)\\ f_\pi^0 &= (1-P_2)P_3 && (5.8)\\ f_\eta &= (1-P_2)(1-P_3) && (5.9)\\ & && (5.10) \end{aligned}$$

where $0 < P_i < 1$ and the P_i's are the actual fitted parameters.

After the statistical uncertainties were extracted, the total error can be estimated by the fact that the excess of χ^2 is due to the underestimation of the errors from the Monte Carlo distributions fitted to the data.

$$\sigma_{total} = \sigma_{statstical} \times \sqrt{\frac{\chi^2}{DOF}} \tag{5.11}$$

where DOF is the number of degrees of freedom of the fit.

The $\log(EM1/ETOT)$ distributions of data at various E_T bins and the corresponding fits are shown in figures 5.9 and 5.10.

Figure 5.11 shows that the $\log(EM1/ETOT)$ distributions of electrons from RUN 1A W and Monte Carlo (E_T = 43.4 GeV) samples do have similar shapes. In the compared W sample we applied the following tight electron selection cuts,

$$1.6 < |\eta| < 2.5$$
$$numberofjets < 1$$
$$E_T(missing) > 25GeV$$
$$E_T(electron) > 25GeV$$
$$0 < dE/dX < 1.5(1MIP)$$
$$Numberoftracks = 1$$
$$Track\_Match\_Significance < 5.$$

5.4 Ionization - dE/dX Method

Because photons have a finite probability to convert within the detector material and produce electron position pairs, another possible way of extracting the photon purities is to measure the relative differences of conversions of direct photons and background particles. Since the decay products of background particles π^0's and η's have two photons, it is expected that they are twice as likely to convert as a single direct photon. Because there is no magnetic field in the central tracking region, the conversion electron and positron pairs appear as a single particle within the DØ detector resolution. Full reconstruction of the conversion pairs is not possible. However, the DØ central tracking chambers sample the track ionization up to 32 times in the forward region. Conversion pairs produce twice the dE/dX of single minimum ionizing particles (MIPs). Using this ionization measuring capability, we

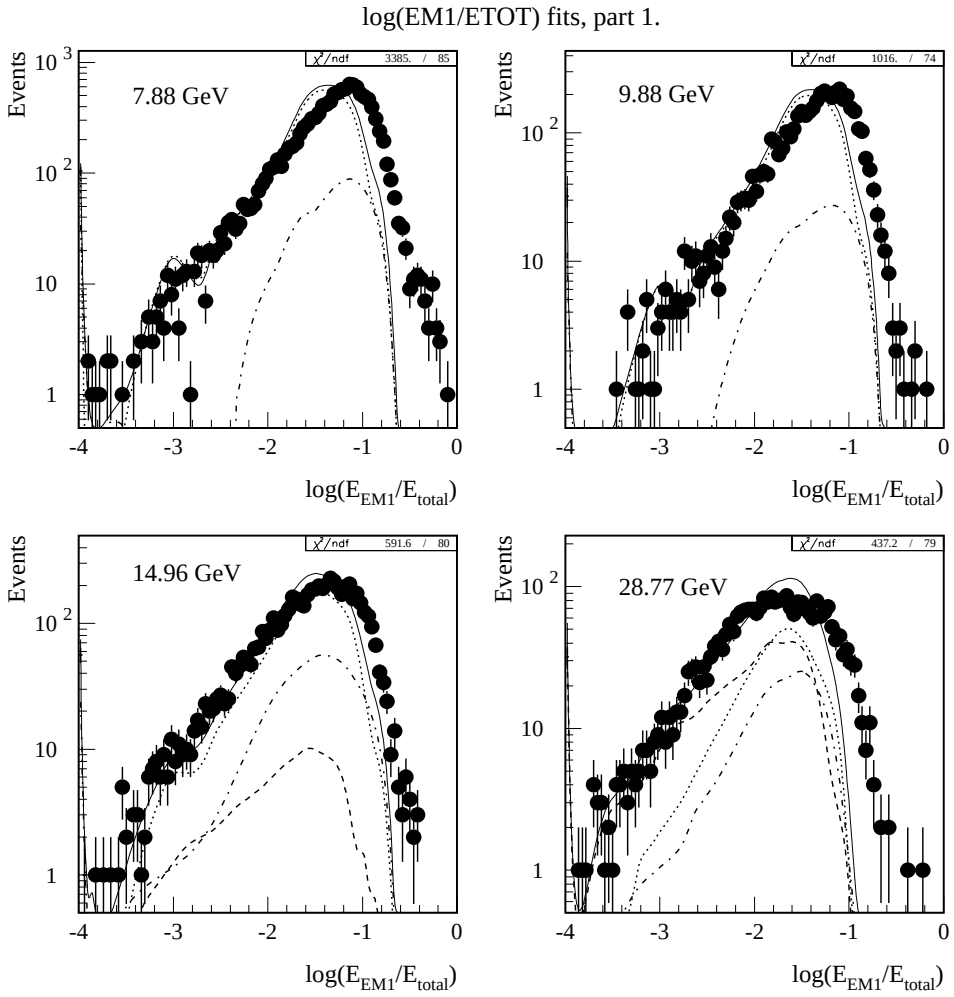

Figure 5.9: The $\log(EM1/ETOT)$ distributions of data (filled circle with error bars) and Monte Carlos (lines), for E_T bins at 7.88, 9.88, 14.96, and 28.77 GeV. The solid line is the sum of the fitted particle fractions. The dotted, dashed, and dash-dotted lines are the contributions from photons, π^0's, and η's.

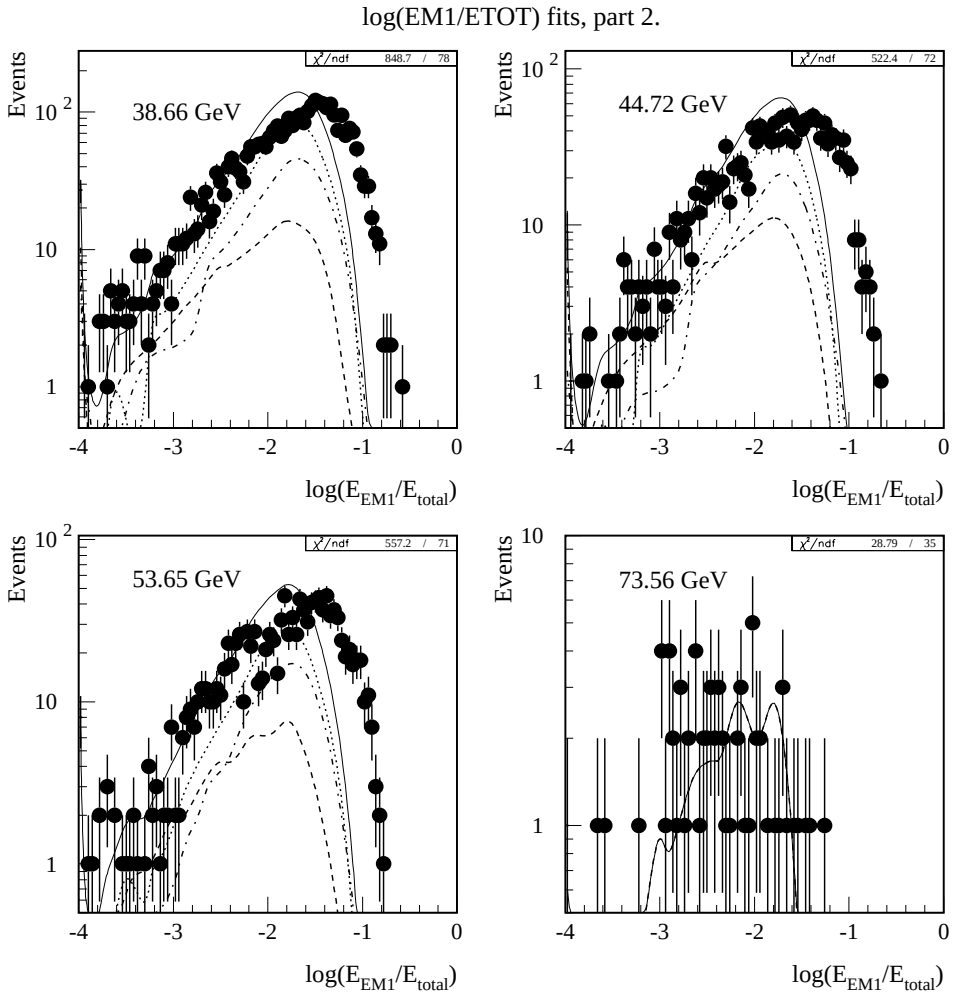

Figure 5.10: The $\log(EM1/ETOT)$ distributions of data (filled circle with error bars) and Monte Carlos (lines), for E_T bins at 38.66, 44.72, 53.65, and 73.56 GeV. The solid line is the sum of the fitted particle fractions. The dotted, dashed, and dash-dotted lines are the contributions from photons, π^0's, and η's.

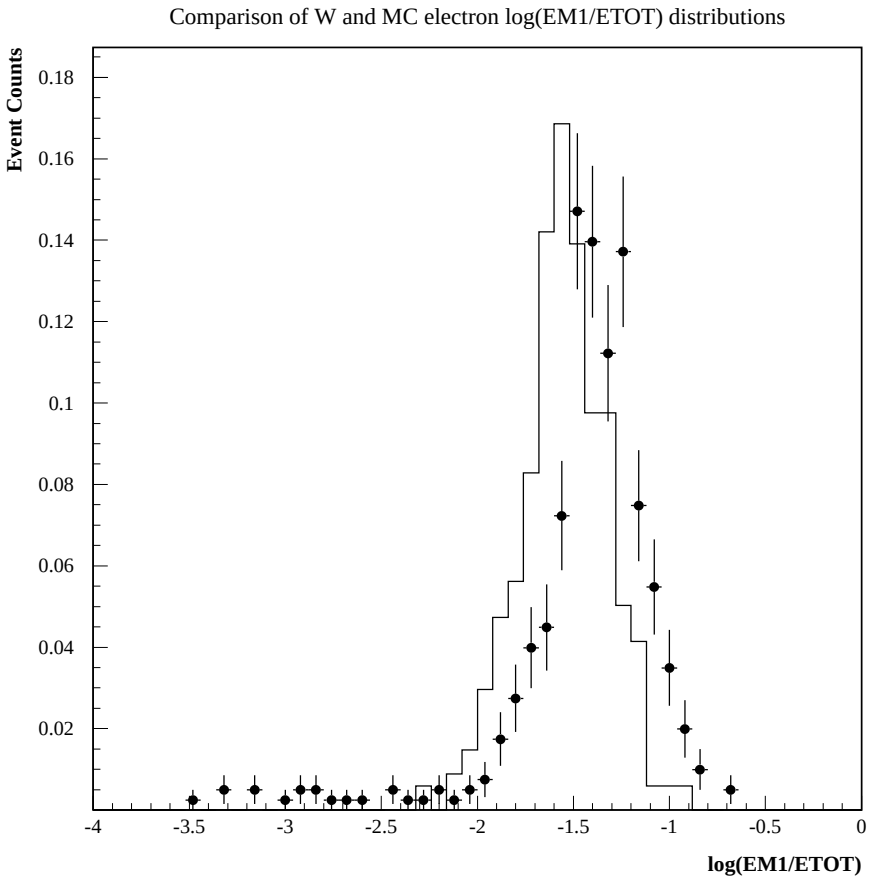

Figure 5.11: The $\log(EM1/ETOT)$ distributions of W sample and Monte Carlo electrons. Average E_T of the electrons is at 43.3 GeV.

can estimate the relative fractions of photons and backgrounds by measuring the dE/dX distribution.

The reconstructed direct photon candidates taken during RUN 1A did not distinguish between candidates with tracks from those without tracks. A candidate is accepted as a possible photon as long as it is consistent with the electromagnetic calorimeter profiles of photons. The event subsample with tracks is then studied with its ionization deposited in the tracking detectors used as the measure of the photon purity extraction.

Figure 5.12 shows examples of dE/dX distributions of the converted photon candidates for four E_T trigger regions. The data shows the contributions from singly and doubly minimum ionizing particles. These are raw distributions and include a 1-MIP peak mostly from background and conversions in which one of the converted electron positron pair escapes detection. The off-line selection cuts will remove a great portion of the 1-MIP part of the distributions as they require good quality EM candidates and tight matching between EM clusters and charged tracks.

5.4.1 Ionization Processes and the Measurement of dE/dX

The amount of ionization, or dE/dX, was measured from the *hits* that were associated with charged particle tracks. The tracking software system for the Central Tracking Detectors found all possible hits along track-finding roads, and fit these hits to form possible track segments. The ionization of a track is really a truncated average of the lower 75% of the pulse heights of the hits that were used for the tracks. The truncated average pulse height is converted to MIP units (normalized to the ionizations from minimum-ionizing particles).

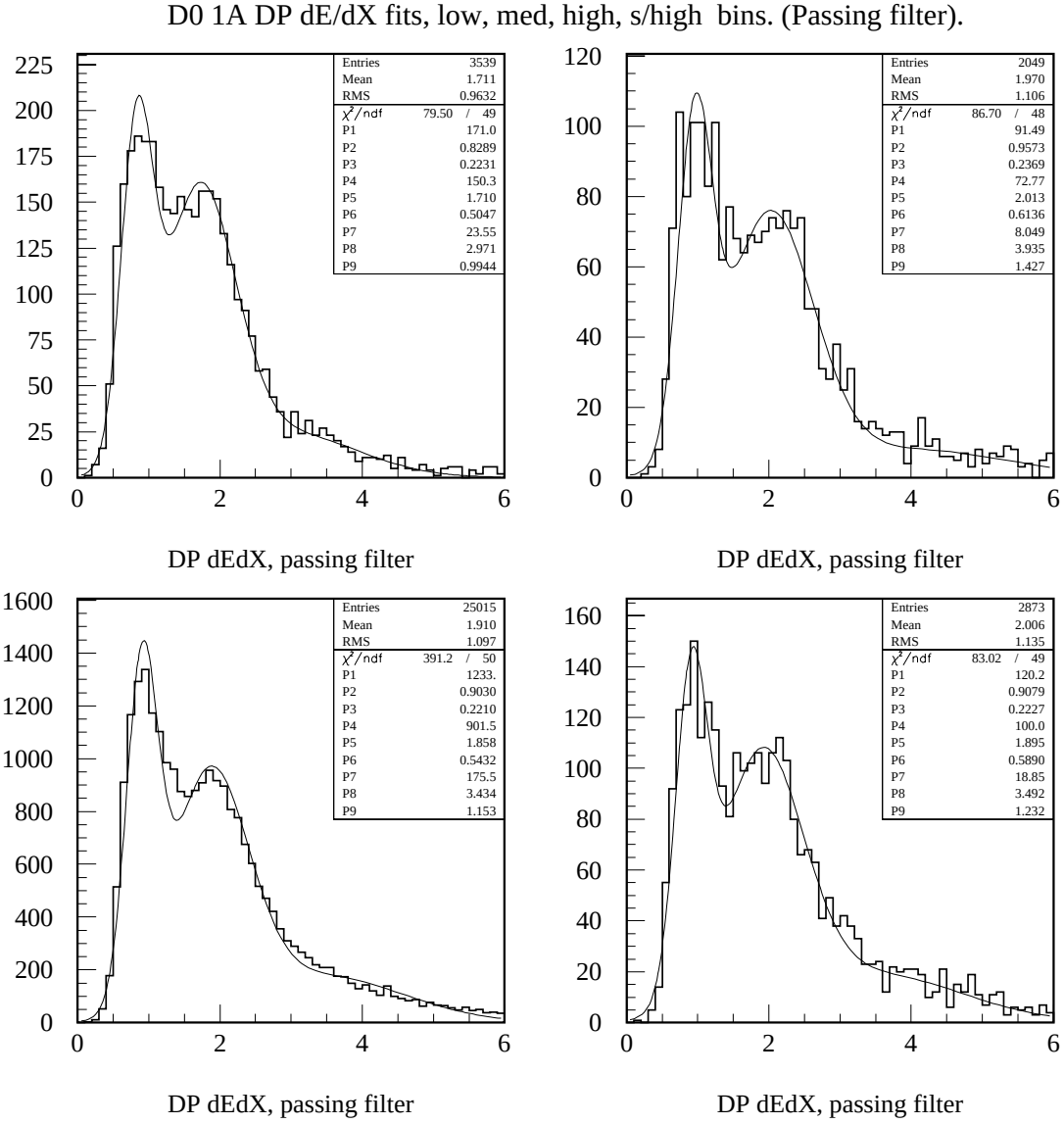

Figure 5.12: The dE/dX distributions for various E_T regions of 13, 26, 44, and 60 GeV for photon candidates passing their corresponding photon filters.

5.4.2 Layering of the Processes and Matrix Formulations

We proceed with the description of the dE/dX-matrix method of photon purity estimation as a particle would when it enters the detector. As particles go through the detector, they experience various transformations which are characterized by the matrix formulation described below. We start with a set of photons, π^0's and η's with definite relative fractions. This set is written as a vector which is transformed by possible decays and conversions to reach a a set of directly measurable states. These states have possible 0, 1, 2, .. to 8 MIP registered in the tracking chamber.

First, if the particle is a π^0or η, it has a certain probability to decay and have one of its two photons escape detection, ie., the two decay photons subtend an angular region in η and ϕ space which is greater than the EM candidate identification road size, 0.2 x 0.2 . These processes are characterized as a 9-by-9 *decay matrix* acting on a 9-element column vector containing the fraction of pure particle states as its elements and results in a 9-element column vector containing the fractions of photons, electrons, photon-pairs as its elements.

$$\begin{pmatrix} \gamma \\ e \\ \gamma\gamma \\ 0 \\ 0 \\ 0 \\ 0 \\ 0 \\ 0 \end{pmatrix} = \begin{pmatrix} 1 & 0 & 0 & 0 & 0 & 0 & 0 & 0 & 0 \\ 0 & 1 & 0 & 0 & 0 & 0 & 0 & 0 & 0 \\ 0 & 0 & 1-r & 0 & 0 & 0 & 0 & 0 & 0 \\ 0 & 0 & 0 & 1 & 0 & 0 & 0 & 0 & 0 \\ 0 & 0 & 0 & 0 & 1 & 0 & 0 & 0 & 0 \\ 0 & 0 & 0 & 0 & 0 & 1 & 0 & 0 & 0 \\ 0 & 0 & 0 & 0 & 0 & 0 & 1 & 0 & 0 \\ 0 & 0 & 0 & 0 & 0 & 0 & 0 & 1 & 0 \\ 0 & 0 & 0 & 0 & 0 & 0 & 0 & 0 & 1 \end{pmatrix} \begin{pmatrix} \gamma \\ e \\ \pi^0/\eta \\ 0 \\ 0 \\ 0 \\ 0 \\ 0 \\ 0 \end{pmatrix}$$

In the decay matrix r is the probability that a background particle decays to a photon pair with opening angle greater than the EM candidate finding road.

Next, we need to take into account that the underlying events may have either

a neutral or charged particle overlapping the EM candidate road which may cause some mis-identifying of the candidates. Charged particles, in the road, will cause the photon candidate to be tagged as an electron. On the other hand, neutral particles, which convert within the road, will leave a track and confuses the photon identification process. In the following second and third matrices of our matrix formulation, we include these two effects – neutral and charged meson overlapping, and assume that their magnitudes are equal. We write down the following matrix equations in the same spirit of the previous one with the column vectors understood to carry the various particle type fractions.

For neutral particles to overlap, assuming that v is the overlap probability, the matrix is

$$\begin{pmatrix} \gamma \\ e \\ \gamma\gamma \\ \gamma v \\ ev \\ \gamma\gamma v \\ 0 \\ 0 \\ 0 \end{pmatrix} = \begin{pmatrix} 1-v & 0 & 0 & 0 & 0 & 0 & 0 & 0 & 0 \\ 0 & 1-v & 0 & 0 & 0 & 0 & 0 & 0 & 0 \\ 0 & 0 & 1-v & 0 & 0 & 0 & 0 & 0 & 0 \\ v & 0 & 0 & 1 & 0 & 0 & 0 & 0 & 0 \\ 0 & v & 0 & 0 & 1 & 0 & 0 & 0 & 0 \\ 0 & 0 & v & 0 & 0 & 1 & 0 & 0 & 0 \\ 0 & 0 & 0 & 0 & 0 & 0 & 1 & 0 & 0 \\ 0 & 0 & 0 & 0 & 0 & 0 & 0 & 1 & 0 \\ 0 & 0 & 0 & 0 & 0 & 0 & 0 & 0 & 1 \end{pmatrix} \begin{pmatrix} \gamma \\ e \\ \gamma\gamma \\ 0 \\ 0 \\ 0 \\ 0 \\ 0 \\ 0 \end{pmatrix}$$

For charged particles to overlap, assuming o is the overlap probability, the matrix is

$$\begin{pmatrix} \gamma \\ e \\ \gamma\gamma \\ 0 \\ 0 \\ 0 \\ \gamma_o \\ e_o \\ \gamma\gamma_o \end{pmatrix} = \begin{pmatrix} 1-o & 0 & 0 & 0 & 0 & 0 & 0 & 0 & 0 \\ 0 & 1-o & 0 & 0 & 0 & 0 & 0 & 0 & 0 \\ 0 & 0 & 1-o & 0 & 0 & 0 & 0 & 0 & 0 \\ 0 & 0 & 0 & 1 & 0 & 0 & 0 & 0 & 0 \\ 0 & 0 & 0 & 0 & 1 & 0 & 0 & 0 & 0 \\ 0 & 0 & 0 & 0 & 0 & 1 & 0 & 0 & 0 \\ o & 0 & 0 & 0 & 0 & 0 & 1 & 0 & 0 \\ 0 & o & 0 & 0 & 0 & 0 & 0 & 1 & 0 \\ 0 & 0 & o & 0 & 0 & 0 & 0 & 0 & 1 \end{pmatrix} \begin{pmatrix} \gamma \\ e \\ \gamma\gamma \\ 0 \\ 0 \\ 0 \\ 0 \\ 0 \\ 0 \end{pmatrix}$$

The above two overlap matrices do not commute, and the order in which they are to be multiplied is important. Therefore, we take the symmetrized sum of the two and use it as the combined overlap matrix.

Furthermore, we need to include the finite conversion probabilities for photons and the neutral mesons. This directly affects the probabilities for the candidates to be detected in the Forward Drift Chamber as converted tracks. Taking the simplest case of a π^0 as an example and assuming that the probability for a single photon to convert in the material in front of the chamber is p, we need to calculate the probabilities of detecting 0, 1, or 2 of the conversion electrons or positrons from the decaying π^0 . Since the two photons from the π^0 are independent in their conversions, the probability that both convert is,

$$p^2$$

and the probability for only one conversion is,

$$2p(1-p)$$

so the probability for at least one conversion is,

$$2p - p^2 \ .$$

In the following matrix, this effect is included for each particle category to calculate the corresponding probabilities that the particle convert to electrons or positrons,

$$\begin{pmatrix} c_0 \\ c_1 \\ c_2 \\ c_3 \\ c_4 \\ c_5 \\ c_6 \\ c_7 \\ c_8 \end{pmatrix} = \begin{pmatrix} 1-p & 0 & (1-p)^2 & 0 & 0 & 0 & 0 & 0 & (1-p)^3 \\ 0 & 1 & 0 & 1-p & 0 & (1-p)^2 & 1 & 0 & 0 \\ p & 0 & 2p(1-p) & 0 & 1 & 0 & 0 & 0 & 3p(1-p)^2 \\ 0 & 0 & 0 & p & 0 & 2p(1-p) & 0 & 0 & 0 \\ 0 & 0 & p^2 & 0 & 0 & 0 & 1 & 0 & 3(1-p)p^2 \\ 0 & 0 & 0 & 0 & 0 & p^2 & 0 & 0 & 0 \\ 0 & 0 & 0 & 0 & 0 & 0 & 0 & 0 & p^3 \\ 0 & 0 & 0 & 0 & 0 & 0 & 0 & 0 & 0 \\ 0 & 0 & 0 & 0 & 0 & 0 & 0 & 0 & 0 \end{pmatrix} \begin{pmatrix} \gamma \\ e \\ \gamma\gamma \\ \gamma v \\ ev \\ \gamma\gamma v \\ \gamma_o \\ e_o \\ \gamma\gamma_o \end{pmatrix}$$

Since the track identification probability is not 100% efficient, we need to include the tracking efficiency as the t parameter in the following matrix,

$$\begin{pmatrix} n_0 \\ n_1 \\ n_2 \\ n_3 \\ n_4 \\ n_5 \\ n_6 \\ n_7 \\ n_8 \end{pmatrix} = \begin{pmatrix} 1 & 1-t & 1-t & 1-t & 1-t & 1-t & 1-t & 1-t & 1-t \\ 0 & t & 0 & 0 & 0 & 0 & 0 & 0 & 0 \\ 0 & 0 & t & 0 & 0 & 0 & 0 & 0 & 0 \\ 0 & 0 & 0 & t & 0 & 0 & 0 & 0 & 0 \\ 0 & 0 & 0 & 0 & t & 0 & 0 & 0 & 0 \\ 0 & 0 & 0 & 0 & 0 & t & 0 & 0 & 0 \\ 0 & 0 & 0 & 0 & 0 & 0 & t & 0 & 0 \\ 0 & 0 & 0 & 0 & 0 & 0 & 0 & t & 0 \\ 0 & 0 & 0 & 0 & 0 & 0 & 0 & 0 & t \end{pmatrix} \begin{pmatrix} c_0 \\ c_1 \\ c_2 \\ c_3 \\ c_4 \\ c_5 \\ c_6 \\ c_7 \\ c_8 \end{pmatrix}$$

The preceding matrix formulation is evaluated with the **MAPLE V** [37] symbolic mathematical package with various efficiencies and MIP fractions determined from the Monte Carlo and RUN 1A collider data sets. The mathematical formulation was also double-checked to ensure overall uniformity of the combined matrix which is the product of all 5 matrices by checking that all fractions add up to unity. This formulation provides the photon purity value at each E_T point.

5.4.3 dE/dX Resolution

The dE/dX information provided by the tracking chambers are truncated average pulse areas normalized to the MIP units for the hits associated with charged particle tracks. The truncation which removed the largest 25% of the hits on the track was necessary to reduce the contributions from the *Landau tails* caused mainly by delta-rays [38]. From test beam studies, the forward drift chamber was reported to have a dE/dX resolution of 13.3% and the capability to separate doubly-ionizing particles from singly-ionizing particles with a rejection ratio of 85 at 97% efficiency [20].

Various environmental factors, like variations in atmospheric pressure, temperature, and chamber gas concentration fluctuations, affect the dE/dX resolution of the forward drift chamber. Corrections for these variations were done by monitoring the behavior of these effects and applying the correction factors in the DØ reconstruction program. However, more long-term variation of the pulse areas still remain.

The dE/dX resolution is further smeared by various processes like bremsstrahlung and multiple scattering as particles travel through the detector material [39]. The net effect is that some portion of the 1 MIP particles will have dE/dX values greater than 1, and some 2-MIP particles loose some of their ionization energy and appear to be slightly less than 2 MIP. The dE/dX is also affected by radiation damage to the tracking detectors. All the above factors combine to smear the dE/dX resolution, as shown in figure 5.13.

To use the dE/dX method for photon purity estimation, it is crucial to be able to estimate the relative fractions of the 1 and 2 MIP peaks. We fit multiple Gaussian functions to the dE/dX distributions and extract the 1 and 2 MIP fractions as the relative size of the areas under each peak.

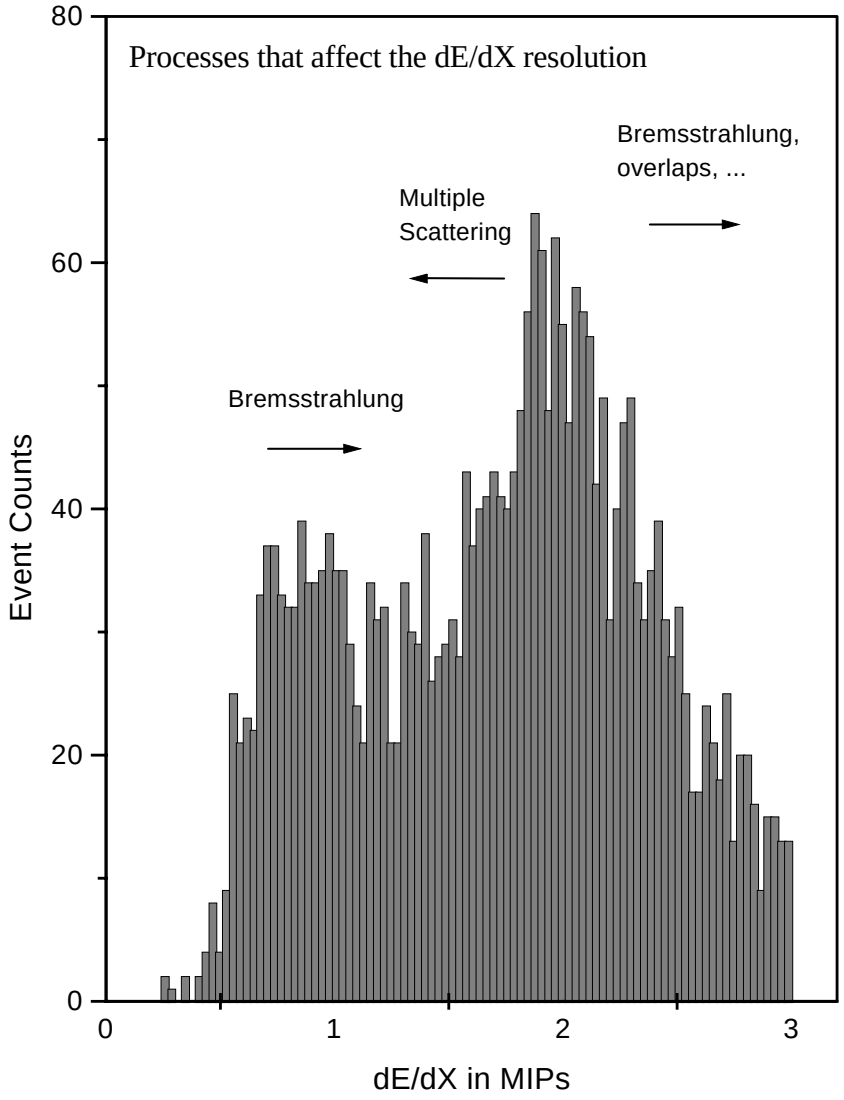

Figure 5.13: Various effects that can smear the tracking chamber dE/dX resolution.

5.4.4 Photon Purity Extraction

When we have included the photon and background particle conversion schemes within the subdetector, we can use the above matrix model to extract the photon purities at various E_T values using the following strategy :

1. Use the RUN 1A W and Z data subsamples to estimate the amount of neutral and charged particle overlapping probabilities.

2. Use a set of Monte Carlo single particle simulations to calculate the photon conversion probability within the detector up to the front wall of the forward drift chamber, since the particle fractions and the MIP fractions are both known at this stage.

3. Apply the previous procedure in reverse, by using the measured MIP fractions of the data at each p_T value chosen and multiplying the conversion matrix in reverse to extract the corresponding photon purity.

The MIP fractions at various E_T regions were obtained by applying constrained multiple Gaussian fits to the dE/dX distributions. The fits shown in figure 5.14 are for the 4 E_T regions investigated.

Due to the fact that the Monte Carlo data samples were generated at fixed E_T 's, 13, 26, 44, and 60 GeV, and these do not exactly match the average E_T values from the direct photon data sample in each trigger region, a linear interpolation was needed to match the Monte Carlo E_T bins to the data E_T bins.

The photon purities as extracted from the dE/dX method are not stable at this moment. The purity values are dependent on the selection cut values and the E_T binning. The MIP fractions are also not very well understood since the boundary between 1 MIP and 2 MIP is not unambiguously defined. As a result, we will present

only the photon purities provided by the EM1 fitting method. Some consideration about possible causes for dE/dX measurement degradation is given in the next section.

5.5 Detector Aging Issues

The Forward Drift Chamber has been located in the DØ collision hall since the beginning of Collider RUN 1A in early 1992, and has been exposed to high radiation during the years of 1992-1995. The amount of radiation induced charge deposited on the sense wires degrades the pulse gains and has had an impact on the chamber performance, especial in ionization (dE/dX) measurements.

As the data were taken, an on-line processing software *CD_HISTOGRAM_EXAMINE* package periodically took a sampling of the events and processed them for monitoring purposes. The pulse areas on each channel were histogramed and kept separately in data files. These pulse area histograms were later studied as a function of integrated luminosity since it is proportional to the amount of radiation seen by the chamber. A gradual performance degradation has been observed. The most serious degradation occured for cells at highest pseudorapidity.

This long term degradation in the chamber gain and pulse areas, together with a few minor short term fluctuations due to high voltage supply or gas problems, affects our capability of using an absolute magnitude of ionization as the dividing line for discriminating between 1 and 2 MIP's, or to use the fitted shape of dE/dX distributions to get the relative MIP fractions. This complicates the already uncertain ionization method for photon purity extraction.

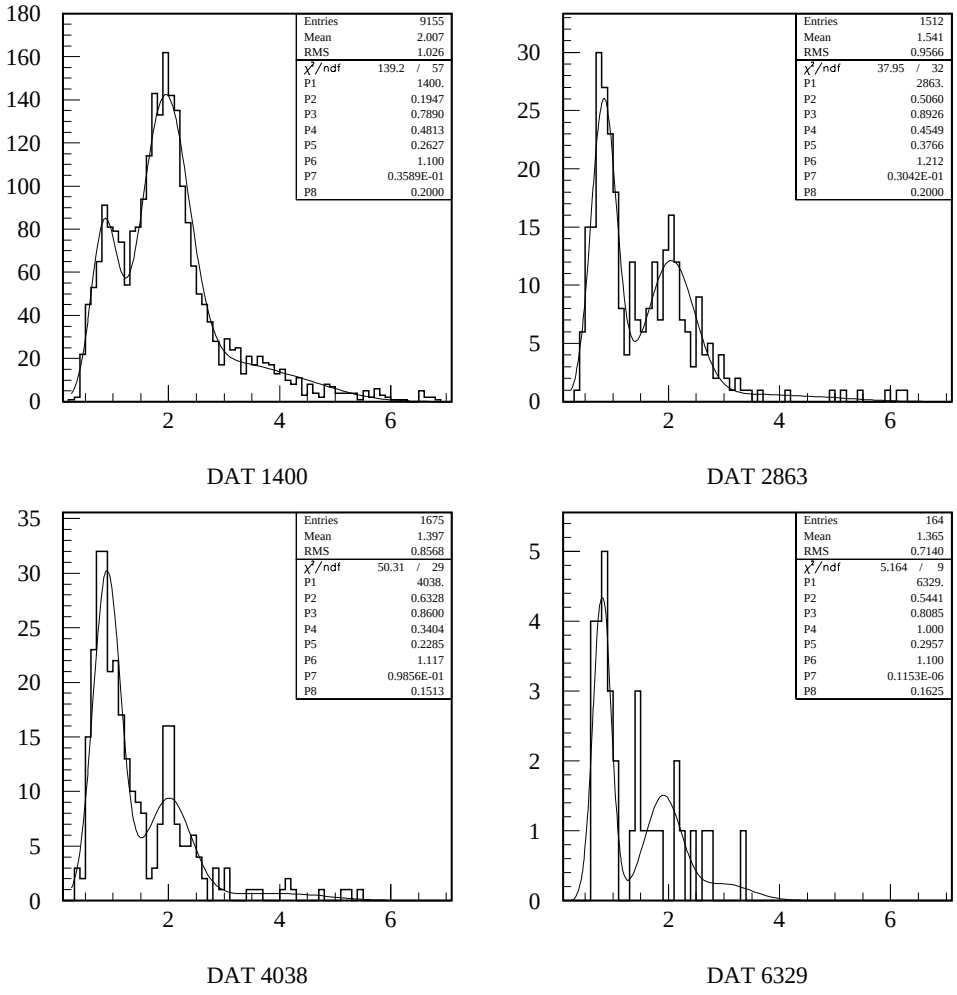

Figure 5.14: Multiple Gaussian fits used to extract MIP fractions, for E_T bins centered at 14.0, 28.63, 40.38, and 63.29 GeV.

Chapter 6

Results, Remarks, and Outlook

6.1 Summary of Cross Section Measurements

The measurement of the forward direct photon production cross section is difficult because it is made in a region of high particle multiplicities and the forward detector is shadowed by a large amount of material which contributes a substantial number of conversions. The central region does not suffer as much from these difficulties [40]. The forward region also sees a higher percentage of beam related backgrounds because it is located closer to the beam pipe. The overall effect is that techniques to extract the photon purity in the central region could simply not be adopted easily in the forward region.

Figure 6.1 shows the raw photon E_T distribution with integrated luminosity, detector acceptance, and cut efficiency included to normalize the distribution. This indicates a smooth distribution with small statistical errors. In this figure no attempt is made to separate background and direct photon signals.

A preliminary photon purity estimation, as obtained from the χ^2 fits to the EM1 distributions, is given in figure 6.2. The errors shown are the total errors which are mainly from the statistical uncertainties of the fits scaled up by the χ^2 per degree

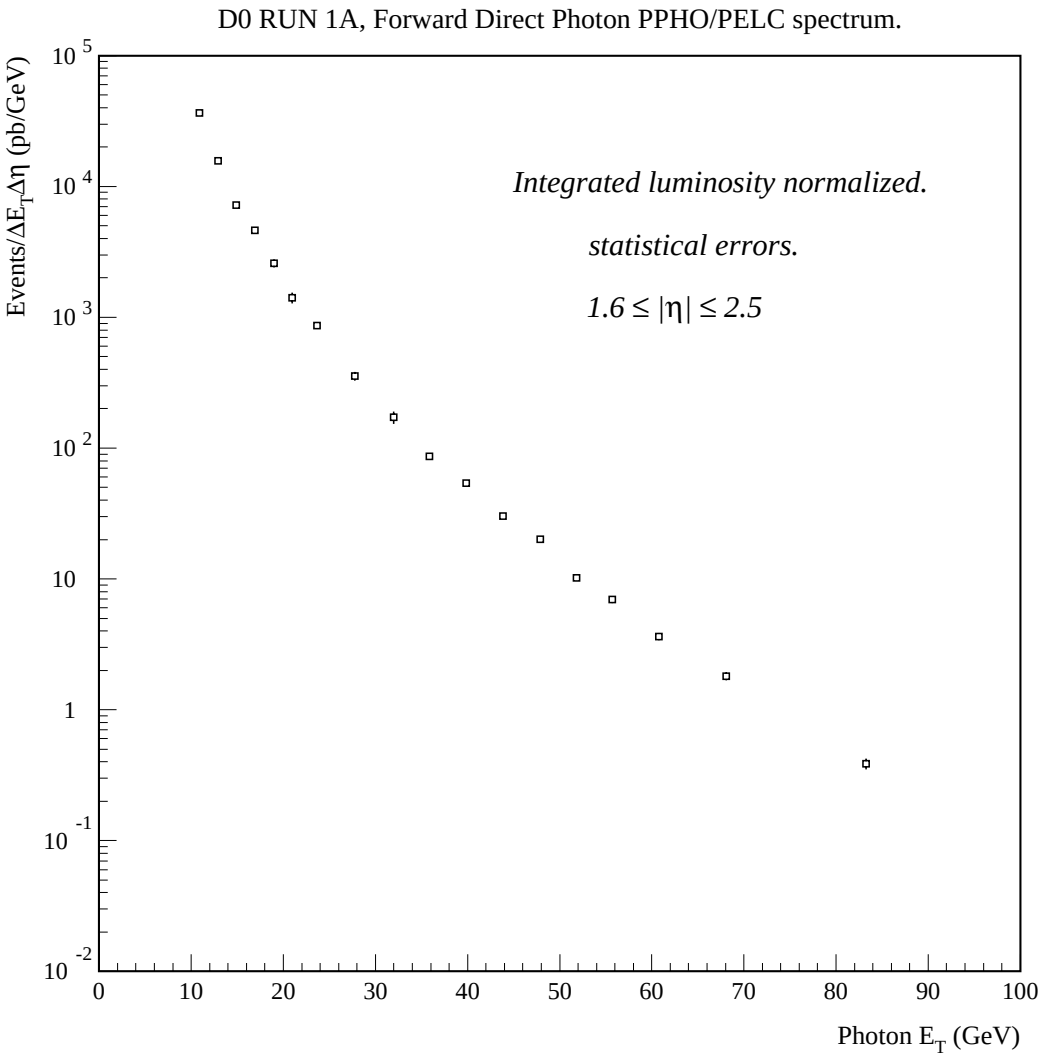

Figure 6.1: The E_T distribution of forward direct photons, after selection cuts and normalized by integrated luminosity. Photon purity corrections have not yet been included.

of freedom for the fitting procedures. This corrects for the underestimation of the total errors by the Monte Carlo samples used in the fits as described in the previous chapter. The figure includes a fit to the function $1 - P_1 e^{-P_2} X$ which will be used as the correcting function for photon purities. The fitting errors and their correlation are used to predict the photon purity and the corresponding error at any E_T point.

Applying these photon purity corrections and calculating the cross section, we obtain the background subtracted E_T distribution of the forward photons as shown in figure 6.3. The superimposed theoretical curve of this figure is discussed in section 6.3.

6.2 Errors

The analysis of forward pseudorapidity region photon fractions has been substantially more difficult than in the central region, mainly due to the following reasons :

- Larger amount of material before the detector components used for photon identification. As a result, the conversion probability is higher which results in larger backgrounds.
- Larger track multiplicity per unit area.
- The Monte Carlo $log(E_{EM1}/E_{total})$ distribution do not adequately simulate contributions from the background and underlying events. This causes a larger mismatch at higher $log(E_{EM1}/E_{total})$ values which rules out the possibility of using a fixed value cut for defining photon purities. The fitting method accounts for this effect with larger χ^2 values for the EM1 fits, which propagate to larger systematic uncertainties.

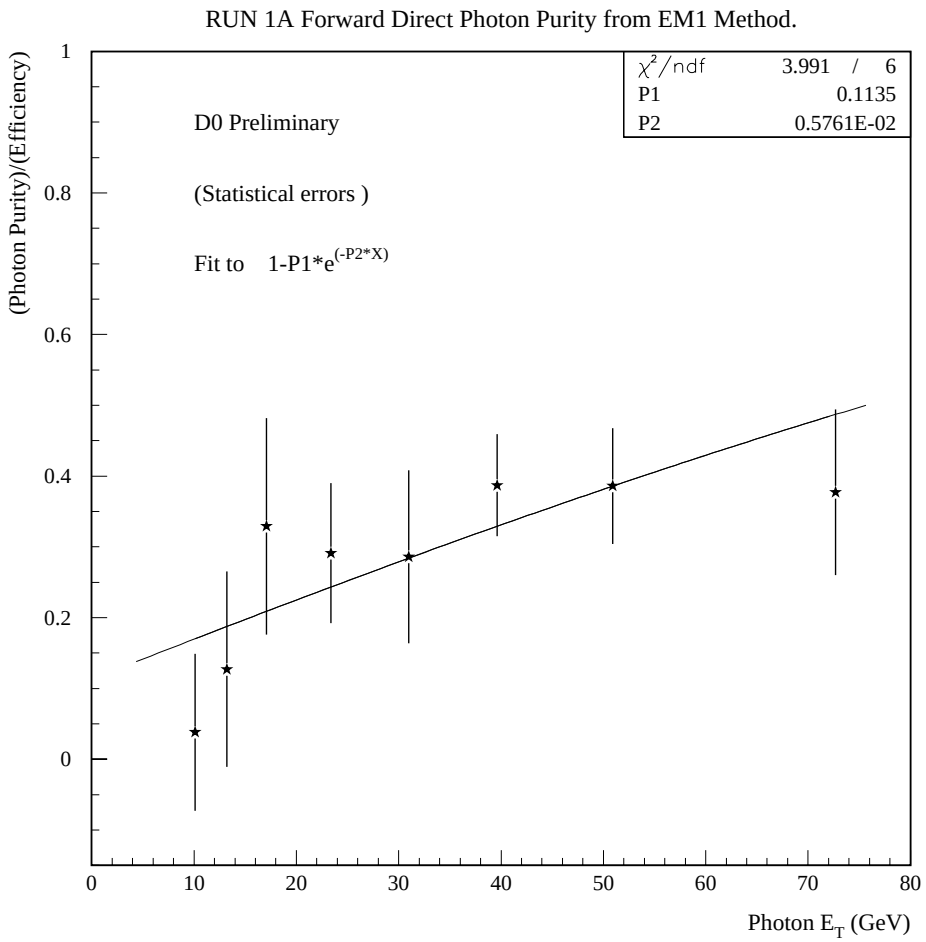

Figure 6.2: Forward photon purity divided by efficiency as given by the EM1 method.

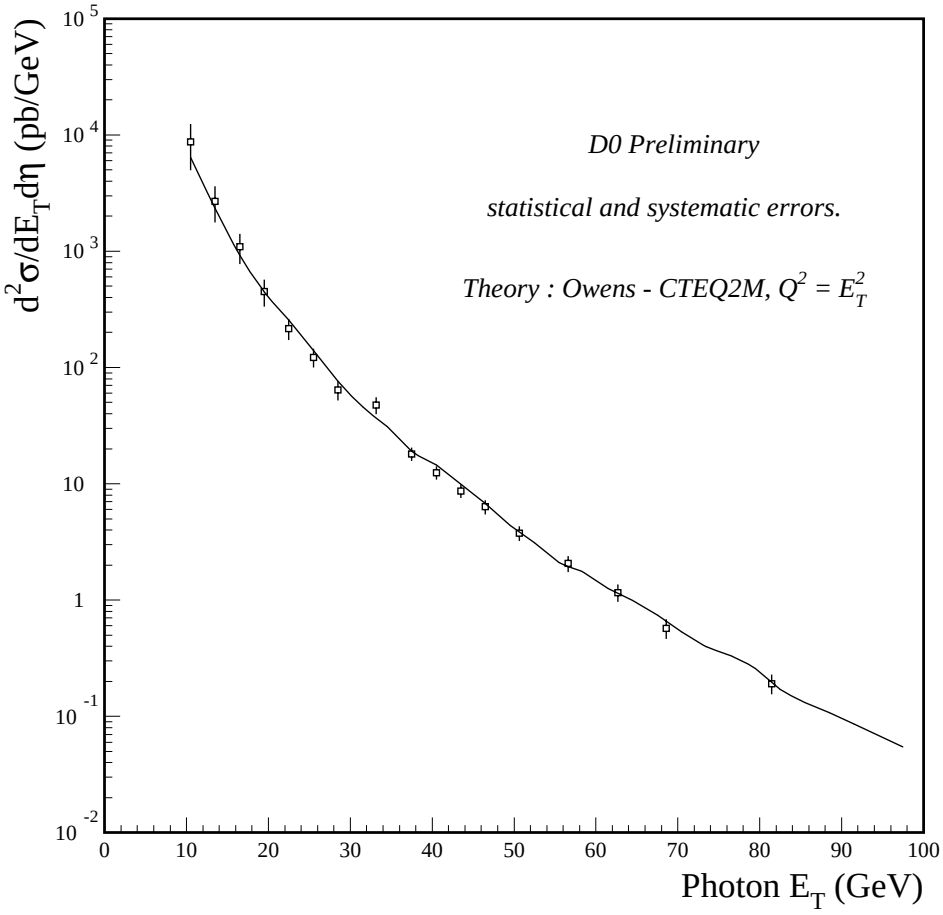

Figure 6.3: The E_T distribution of forward direct photons, after selection cuts, normalization by integrated luminosity, and correction by photon purities. The line is the NLO QCD prediction.

6.3 Predictions from NLO QCD Calculations

For this analysis, we have used the theoretical predictions of the direct photon cross section by Owens et al. [13, 41] for comparison. This is a NLO QCD calculation which includes leading order photon plus jet, and higher order photon plus two jets processes. The anomalous photon production is incorporated by convoluting the di-jet processes by a photon fragmentation function. This theoretical prediction also includes the CTEQ2M parton distribution functions [42]. This prediction of the forward photon E_T distribution is shown in figure 6.4, and as the superimposed curve in figure 6.3.

The steeply falling shape of the cross section is mainly due to the following factors [12] :

- The cross sections of the contributing parton level subprocesses decrease as the E_T of the photons increases.
- The minimum values of the momentum fractions, x_a and x_b, also increase as we go to higher photon E_T , thus entering the region where the parton distribution functions are decreasing rapidly. This contributes further to the decrease of the cross section.
- The photon fragmentation function decreases as we go to higher photon E_T .
- The k_T effect, which will be discussed in section 6.4, may further contribute to the steep fall of the cross section.

Qualitatively, the theoretical predictions match the data well. However, to enhance any differences, figure 6.5 gives a percentage difference between the data and theory in every E_T region. The hatched region is the estimated systematic uncertainty. The forward photon experimental cross section appears steeper than the theoretical prediction in the lower E_T region. In the higher E_T region, it agrees well with theory

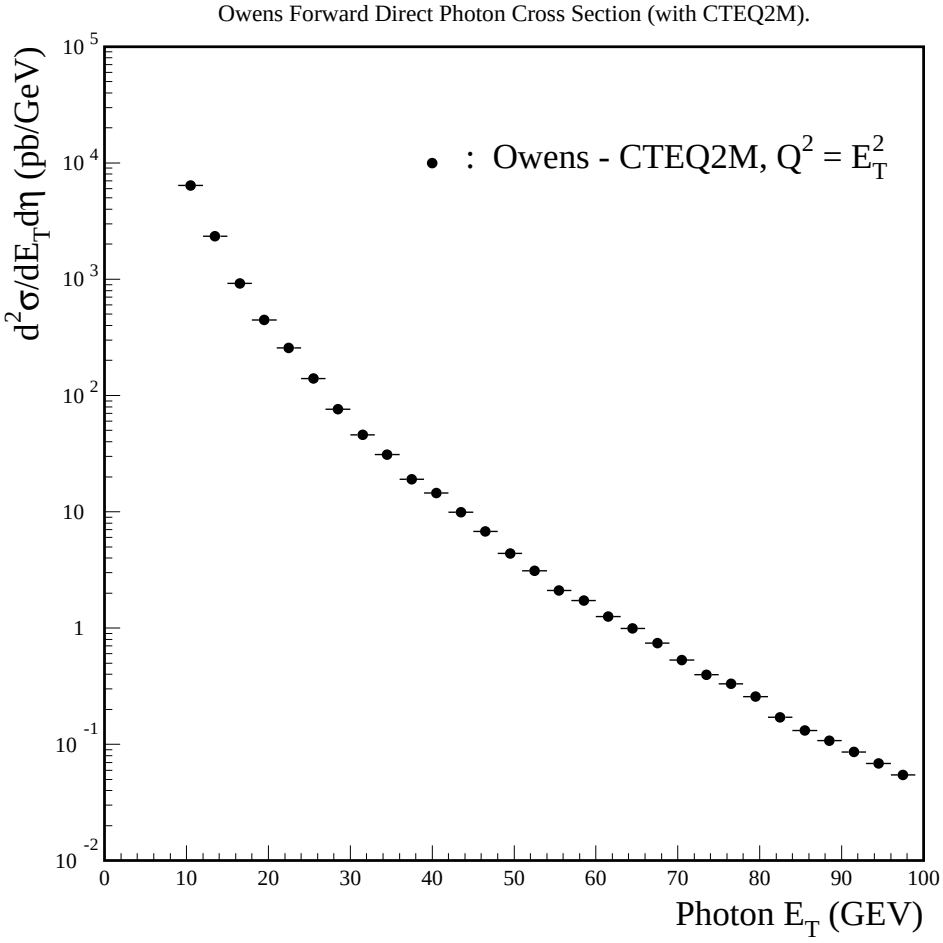

Figure 6.4: The theoretical forward direct photon cross section, as given by the NLO QCD calculations by Owens et al. with CTEQ2M parton distribution functions. The horizontal bars are the E_T bin sizes, not errors on E_T .

within experimental uncertainties. The data point at 33 GeV which is higher than the points on either side corresponds to the transition region between the MEDIUM and HIGH triggers. It is suspected that the normalization may not have properly corrected the data at this point. The estimated errors include our best calculation of this effect.

The difference in the shape of the cross section and the excess of data over theory in the low E_T region has profound implication and is consistent with what we have found in the central pseudorapidity region [43]. The following sections discuss these implications.

6.4 x_T Distributions and Global Comparisons

It has been pointed out by recent QCD global studies [44] that the x_T distributions of direct photon production from various experiments are invariably steeper than NLO QCD predictions at the lower E_T region of each experiment irrespective of their specific x range, as seen in figure 6.6. This discrepancy cannot be accounted for by new global fits of parton distribution functions or improved photon fragmentation functions alone. The experimentally studied x_T range is from 0.01 to 0.6, which is impressively wide. It was suggested that the additional smearing of k_T (transverse momentum of initial state partons with respect to the incoming hadrons) can probably explain this discrepancy [44]. If the initial state partons have some transverse momenta and are not collinear to the hadrons as we have assumed, the transverse motion is passed on to the final state partons and makes their E_T spectrum steeper. This effect is clearly seen in the low E_T region since the amount of k_T is not negligible compared to the total E_T . The k_T smearing is a combination of the following effects :

- The initial state partons are confined within hadrons which are approximately $0.5 fm$ in size. Due to the *uncertainty principle*, they should have some *intrinsic*

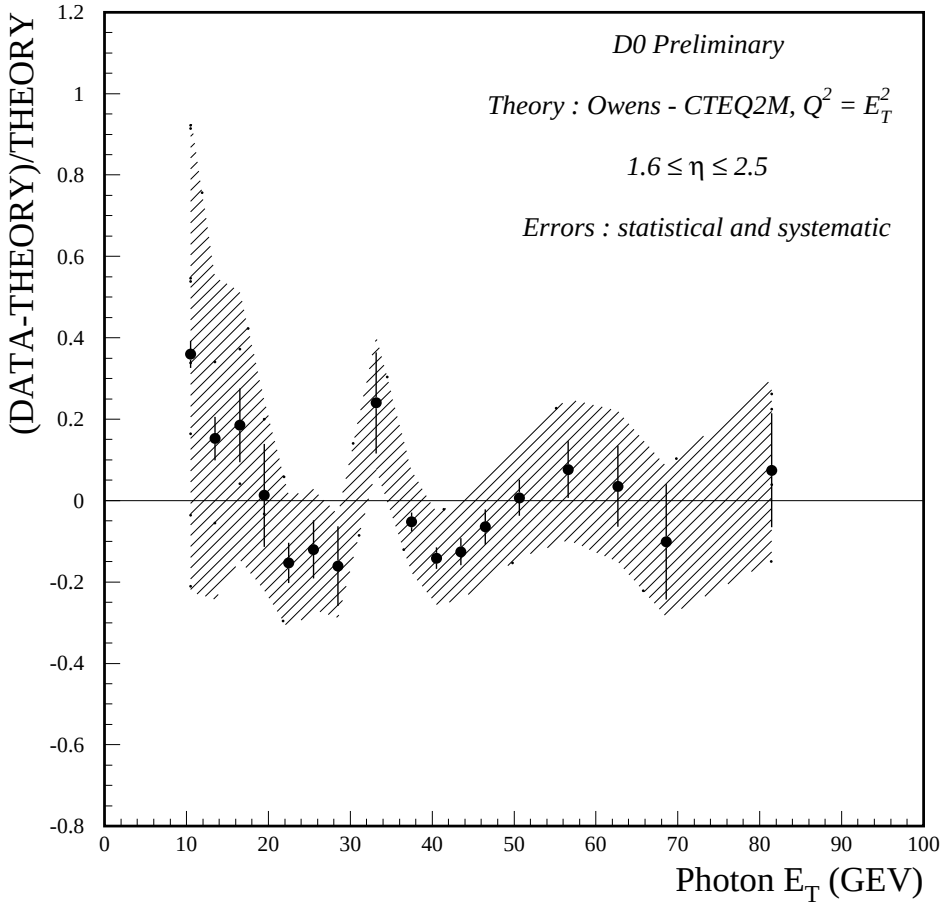

Figure 6.5: Percentage difference between DØ RUN 1A direct photon cross section and the QCD NLO Prediction (Owens et al.) The high point at 33 GeV is at the transition region between two triggers.

transverse momenta around $0.4GeV$.

- The radiation of gluons from initial state partons will give the partons certain transverse momenta. This initial state gluon emission can be the dominant effect contributing to the k_T smearing.

While the phenomenological studies are ongoing, the direct photon data, with the addition of the forward photon results that are available now, can certainly aid in the understanding of the above properties.

The DØ central region photon cross section also shows a similar steepening at low x_T as seen in the other experiments [43]. The x_T region probed is roughly equivalent to the CDF data. With the additional capability of forward photon detection, as described in chapter 2, the minimum values of gluon x being probed now extend the lower region, to roughly $x < 0.02$. As can be seen from figure 6.7, the shape of the forward cross section as a function of x_T also shows a similar steepening as compared to NLO QCD predictions. This is expected since x_T is proportional to p_T. Since experiments are consistent on this rise in the cross section, theoretical models have to be improved to make their predictions consistent with data.

A side note pointed out in chapter 2 is that the theoretical prediction of the photon cross section requires a specific *scale* to be used in the evaluation of the strong coupling constant and parton distribution functions. The comparison of the NLO QCD prediction to the experimental cross section described here employs E_T as the natural choice of scale.

Another test for perturbative QCD using direct photons is the center-of-mass angular distribution. This study has been done in the central pseudorapidity region [45, 46] and found to be in good agreement with NLO QCD. The availability of the forward photon results enables the extension of this analysis into the forward region for future analysis.

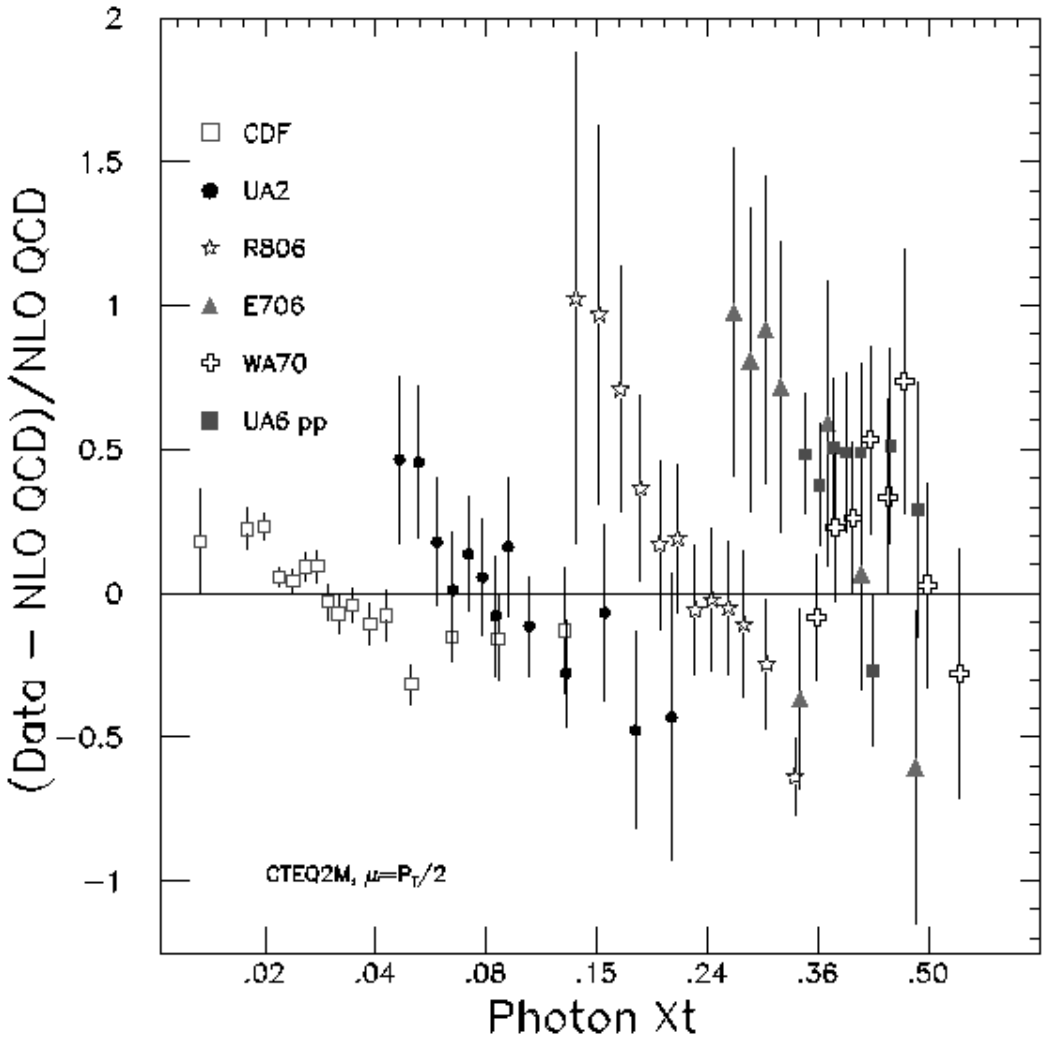

Figure 6.6: x_T distribution comparison of existing direct photon cross section data with the NLO QCD calculations with CTEQ2M parton distribution functions. This figure was extracted from Huston et al., Phys. Rev. D51, 6139 (1995).

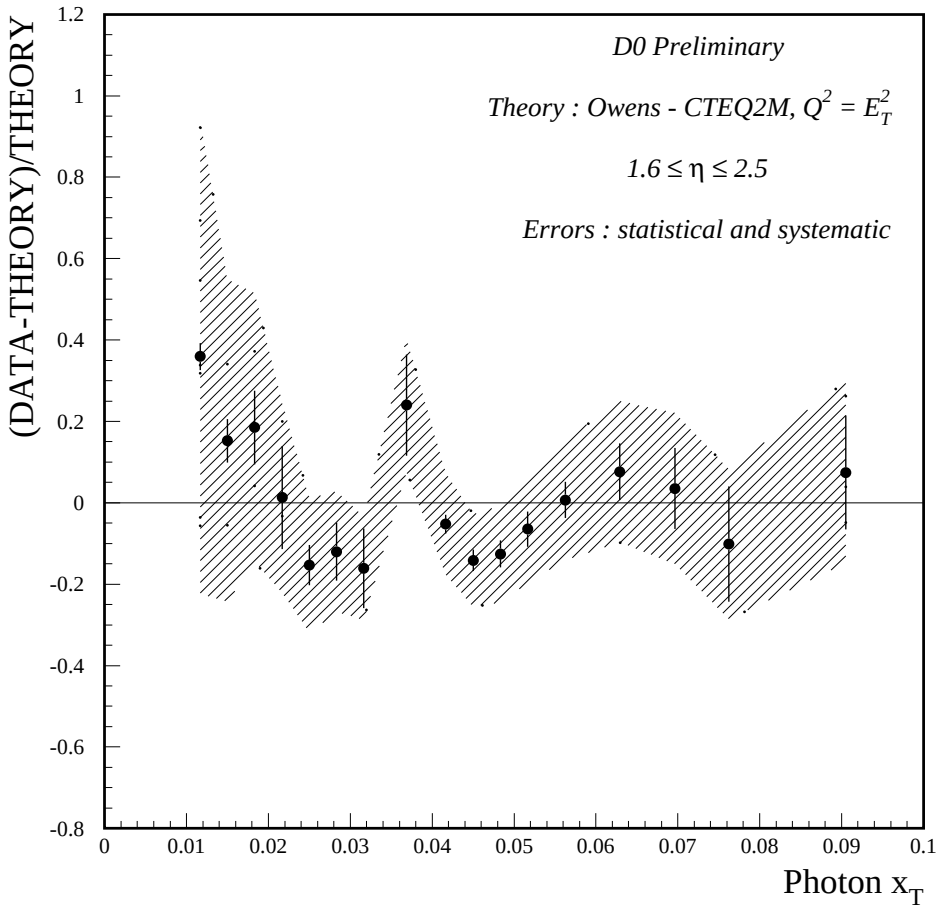

Figure 6.7: Percentage difference between DØ RUN 1A forward direct photon cross section and the NLO QCD prediction as a function of x_T. The high point at 0.036 is at the transition region between two triggers.

6.5 Outlook for RUN 1B Analysis

In Collider RUN 1B, the DØ direct photon trigger configuration was slightly changed, but the data collection strategy remained similar to what was taken in RUN 1A. Special runs were arranged to populate, in particular, the region of lower E_T photon candidates. The runs taken during the years 1993-1995 had higher statistics due to the longer running period and usually higher luminosities. The photon trigger turn-on curve as a function of E_T is currently being studied to improve the uncertainties related to trigger efficiencies, which were not accounted for in the 1A analysis other than early trigger studies and simulation results.

Because the instantaneous luminosities during normal data taking were higher in RUN 1B, the possibility of having multiple interactions has increased. This poses a potential problem for electron/photon identification efficiencies since these particles are fully recognized only if they can be matched with their interaction vertex. The larger charge particle multiplicity is also a factor for tracking chamber resolution degradation. All efficiencies values, therefore, will have to be re-evaluated for a calculation of the direct photon cross section.

However, due to the larger statistics collected during RUN 1B and the capability to extend the cross section measurement up to higher pseudorapidity region, we expect that DØ will play an important role in contributing to further understanding of NLO QCD physics and hadronic structures.

A few items which DØ can investigate or improve compared to the the RUN 1A analysis are listed below.

- Pseudorapidity dependence of direct photon cross sections.
- More detailed studies of trigger/filter turn-on curves. This requires special runs with the photon trigger configurations. These runs are scheduled to be taken during the current collider run period. Another indication of the turn-on can also be estimated by Monte Carlo studies which are currently underway.

- Better consistency checks of photon purities between different estimation methods.
- Generation of more realistic Monte Carlo events to see the detailed activities around the photon candidates.

6.6 Conclusion

We have measured the production cross section of direct photons in the forward pseudorapidity region at the DØ detector. These cross sections agree well with theoretical NLO QCD predictions, except for the lowest E_T region. The steepening of the cross section at lower E_T values is consistent with observations from previous experiments and should be investigated further both experimentally and theoretically.

Bibliography

[1] S. Abachi et al., *Observation of the Top Quark*, *Phys. Rev. Lett.* **74**, 2632 (1995).

[2] R.D. Field, *Applications of perturbative QCD*, (Addison-Wesley, 1989).

[3] CTEQ Collaboration, *Handbook of Perturbative QCD*, Fermilab-Pub-93/094, 1993.

[4] P.D.B. Collins, A.D. Martin, E.J. Squires, *Particle Physics and Cosmology*, (John Wiley & Sons, 1989).

[5] J. Huston, *Direct Photons and Related Topics*, Summer School on QCD Analysis and Phenomenology, Lake Ozark, Missouri, Aug. 10-18, 1994.

[6] J.F. Owens, W.K. Tung, *Parton Distribution Functions of Hadrons*, Fermilab-Pub-9259-T, 1992.

[7] P.D.B. Collins et al., *Hadron Interactions*, (Adam Hilger, 1984).

[8] P. Aurenche et al., *Prompt Photon Production at Colliders*, *Phys. Rev.* **D42**,1440 (1990).

[9] P. Aurenche, P. Chiappetta, M. Fontannaz, J.P. Guillet, E. Pilon, *Next-to-Leading Order Bremsstrahlung Contribution to Prompt Photon Production*, *Nucl.Phys.* **B399**, 34 (1993).

[10] R. Feynman, *Photon-Hadron Interactions*, (Benjamin, 1972).

[11] J.C. Collins, D.E. Soper, *The Theorems of Perturbative QCD*, *Ann. Rev. Nucl. Part. Sci.* **37**, 383 (1987).

[12] J. Owens, *Large-Momentum-Transfer Production of Direct Photons, Jets, and Particles*, *Rev. Mod. Phys.* **Vol. 59, No.2**, 465 (1987).

[13] H. Baer, J. Ohnemus, J.F. Owens, *A Next-to-Leading Logarithm Calculation of Direct Photon Production.* , *Phys. Rev.* **D42**, 61 (1990).

[14] J.P. Ralston, *Pocket Partonometer*, *Phys. Lett.* **B172**, 430 (1986).

[15] H. Weerts, et al., *Summary Report of the QCD Collider Group*, DØ Internal Note 916, 1989.

[16] S. Abachi et al., *The DØ Detector*, *Nucl. Instr. and Meth.* **A338** , 185 (1994).

[17] S. Abachi et al., *The Beam Tests of the D0 Uranium Liquid Argon End Calorimeters*, *Nucl. Instr. and Meth.* **A324** , 53 (1992).

[18] J. Bantly et al., *The Central Tracking Detectors for DØ*, *Nucl. Instr. and Meth.* **A279**, 243 (1989).

[19] D. Claes, C.K. Jung, Y.C. Liu, *Level 2 Trigger Tracking for Electron Filtering*, DØ Internal Note 1229, 1991.

[20] R.E. Avery et al., *Performance of the Forward Drift Chambers for the DØ Detector*, *IEEE Trans. Nucl. Sci.* **40**, 573 (1993).

[21] C. Stewart, *Jets in the DØ Calorimeter*, DØ Internal Note 1516, 1993.

[22] F. Halzen, M. Dechantsreiter, D.M. Scott, *Structure of Direct Photon Events*, *Phys. Rev.* **D22**, 1617 (1980).

[23] S. Hagopian et al., *DØ Event Display Users Guide Pixie V2.1*, DØ Internal Note 941. 1990.

[24] S. Fahey, private communication.

[25] L. Paterno et al., *Change to the D0 Luminosity Monitor Constant*, DØ Internal Note 2401, 1994.

[26] Particle Data Group, *Review of Particle Properties*, *Phys. Rev.* **D50**, 1 (1994).

[27] N. Graf, *DØ Electron ID - the CAPHEL Package*, DØ Internal Note 1302, 1991.

[28] W.R. Leo, *Techniques for Nuclear and Particle Physics Experiments*, (Springer-Verlag, 1987).

[29] S. Abachi, et al., *W and Z Boson Production in $p\overline{p}$ Collisions at $\sqrt{s}$ = 1.8 TeV*, *Phys. Rev. Lett.* **75**, 1456 (1995).

[30] P.M. Grudberg, *Cross Section Measurements of W and Z Bosons to Electrons at DØ : Event Selection and Efficiency Studies*, DØ Internal Note 2316, 1994.

[31] J. Womersley, *Random Charged Track Overlap Probability in the Central and Forward Direct Photon Samples*, DØ Internal Note 2106, 1994.

[32] T. Ferbel, W.R. Molzon, *Direct-Photon Production in High-Energy Collisions*, *Rev. Mod. Phys.* **Vol. 56, No.2**, 181 (1984).

[33] J. Womersley, *Distinguishing Photons from π^0ś in the DØ Calorimeter*, DØ Internal Note 1010, 1991.

[34] A.G. Frodesen et al., *Probability and Statistics in Particle Physics*, (Columbia University Press, 1979).

[35] F. James, *MINUIT Reference Manual*, CERN, Program Library Long Writeup D506, 1994.

[36] S. Linn, *The Photon Purity in the Central Rapidity Region*, DØ Internal Note 2326, 1995.

[37] B.W. Char, et al., *MAPLE V Language Reference Manual*, (Springer-Verlag, 1991).

[38] S. Rajagopalan, Ph.D. thesis, Northwestern University, Evanston, 1992.

[39] W. Blum, and L. Rolandi, *Particle Detection with Drift Chambers*, (Springer-Verlag, 1993).

[40] S. Fahey, *Direct Photon Production at DØ*, DØ Internal Note 2277, 1994.

[41] H. Baer, J. Ohnemus, J.F. Owens, *A Calculation of the Direct Photon Plus Jet Cross-Section in the Next-to-Leading Logarithm Approximation*, *Phys. Lett.* **B234**, 127 (1990).

[42] H.L. Lai et al., *Global QCD Analysis and the CTEQ Parton Distributions*, MSU-HEP-41024, 1994.

[43] S. Linn, DØ Internal Note 2745, 1995.

[44] J. Huston, E. Kovacs, S. Kuhlmann, H.L. Lai, J.F. Owens, W.K. Tung, *A Global QCD Study of Direct Photon Production*, *Phys. Rev.* **D51**, 6139 (1995).

[45] P. Rubinov, Ph.D. thesis, State University of New York, Stony Brook, 1995.

[46] P. Aurenche, R. Baier, M. Fontannaz, D. Schiff, *A QCD Analysis of the Prompt Photon Away-Side Jet Cross Section Measured in pp Collisions*, *Phys. Lett.* **B168**, 441 (1986).